Computational Mechanics
https://doi.org/10.1007/s00466-024-02450-y

ORIGINAL PAPER

Phase field modelling and simulation of damage occurring in human vertebra after screws fixation procedure

Deison Preve[1] · Pietro Lenarda[2] · Daniele Bianchi[3] · Alessio Gizzi[3]

Received: 6 October 2023 / Accepted: 24 January 2024

Abstract
The present endeavour numerically exploits the use of a phase-field model to simulate and investigate fracture patterns, deformation mechanisms, damage, and mechanical responses in a human vertebra after the incision of pedicle screws under compressive regimes. Moreover, the proposed phase field framework can elucidate scenarios where different damage patterns, such as crack nucleation sites and crack trajectories, play a role after the spine fusion procedure, considering several simulated physiological movements of the vertebral body. Spatially heterogeneous elastic properties and phase field parameters have been computationally derived from bone density estimation. A convergence analysis has been conducted for the vertebra-screws model, considering several mesh refinements, which has demonstrated good agreement with the existing literature on this topic. Consequently, by assuming different angles for the insertion of the pedicle screws and taking into account a few vertebral motion loading regimes, a plethora of numerical results characterizing the damage occurring within the vertebral model has been derived. Overall, the phase field results confirm and enrich the current literature, shed light on the medical community, which will be useful in enhancing clinical interventions and reducing post-surgery bone failure and screw loosening. The proposed computational approach also investigates the effects in terms of fracture and mechanical behaviour of the vertebral-screws body within different metastatic lesions opening towards major life threatening scenarios.

Keywords Phase field approach to fracture · Human vertebra · Pedicle screws fixation · Numerical comparison

1 Introduction

Originated from mathematical techniques based on $\Gamma-$convergence [1, 2] and tailored for the approximation of free discontinuity problems [3, 4], the phase field regularization of brittle fracture proposed by Francfort and Marigo [5] has attracted a remarkable attention within the computational fracture mechanics community over the last decade. As compared to other computational methods for damage and fracture simulation in materials and components, such as for instance the crack band model [6], the smeared crack model [7], non-local and diffuse damage models [8, 9], or gradient damage models [10], the phase field approach offers an elegant solution for problems involving linear elastic fracture mechanics. This solution is pursued through an energy minimization which, in the Γ-convergence limit, consistently reproduces the Griffith theory of fracture. The phase field approach to fracture, further analysed in [11, 12], has been applied in a considerable series of works proposing comparisons with other non-local damage models and discussing several detailed aspects regarding the finite element implementation [13–19]. In this context, it is worth recalling the fundamental contribution by Miehe and co-workers [20, 21] that were the first to propose a robust finite element implementation of the phase field for brittle fracture, specialized to account for damage irreversibility and based on a suitable degradation mechanism able to simulate situations involving tensile stress states.

The state-of-the-art literature on phase field models clearly shows that the approach is mature for technical applications. In this regards, Tannè et al. [22] have recently assessed the capabilities of the phase field approach (see in particular the

✉ Pietro Lenarda
pietro.lenarda@imtlucca.it

1 Polytechnic Department of Engineering and Architecture (DPIA), University of Udine, Via delle Scienze 208, 33100 Udine, Italy

2 IMT School for Advanced Studies Lucca, Piazza San Francesco 19, 55100 Lucca, Italy

3 Department of Engineering, Università Campus Bio-Medico di Roma, 00128 Rome, Italy

Published online: 07 March 2024

AT1 and the AT2 models) to predict crack nucleation from V-notches and from points with stress concentrations. Phase field modelling has numerous applications, especially in the field of biomedical engineering, particularly in the study of bone fractures. In this regard, fractures in the vertebrae can be challenging to analyse and treat due to their complex shapes and locations [23, 24]. However, phase field modelling can help by simulating the fracture process and shedding light on the underlying mechanisms involved. In particular, phase field modelling can be used to investigate the impact of vertebral fixation and screw placement on the healing of vertebral fractures. By incorporating the presence of screws and other fixation devices into the simulation, researchers can evaluate the mechanical stability of the fracture site and predict the potential for screw loosening or failure [25]. Additionally, researchers can gain insights into the effects of different placement strategies on the fracture propagation process.

Quantitative and qualitative finite element models are being developed to evaluate damage patterns and predict crack propagation in biological tissues. So much so, recently, the capability of a plethora of phase field implementations for modelling and analysing crack growth in bone tissue has been successfully applied [26–28], thus phase field theory seems a promissory approach to assess bone fracture patterns. In this context, the biomechanical problem of characterizing damage and predicting crack trajectories in a human vertebra after the fixation procedure of pedicle screws (see Fig. 3a) can be tackled utilizing a phase field method.

Screw fixation in vertebral surgery is a critical aspect of spinal procedures aimed at stabilizing the spine, treating fractures, deformities, or degenerative conditions. While advances in medical technology have significantly improved the success rates of these interventions, clinical challenges still exist, leading to cases where the fixation may not work as intended and might need for re-intervention, as, for instance, demonstrated in the X-rays in Fig. 1, with the screw positioning as in [29]. Besides, achieving optimal screw placement to provide stability without compromising nearby structures such as nerves or blood vessels is a delicate balance. Screw types, screw dimensions and insertion pathways can play an important role in clinical interventions, as in in-vitro studies [29, 30]. Figure 2 shows microradiographic images at different fixation techniques placement in the lumbar vertebral interface. To minimize the risk of fixation failure and the need for re-intervention, the present numerical computational model based on the theory of phase field to fracture can considerably contribute to enhance precision and reduce complications of these challenging interventions.

Metallic pedicle screws are used in spine fusion procedures when the intervertebral discs have been damaged by ageing or any trauma, causing the vertebrae to rub against each other and compress the nerves that pass through them. Spinal fusion joins two or more diseased vertebrae together, preventing motion at the vertebral segment. The screws are inserted into the respective pedicle regions, connecting the screws through a vertical rod, providing a means for gripping onto a vertebral segment and limiting its motion, resulting in stable spine fixation. Bone damage and screw loosening may occur due to various post-operative events [32]. Furthermore, the mechanical behaviour of the pedicle screw insertion angle has been experimentally investigated [29, 33]. Nonetheless, finite element analysis allows for the assessment of numerous possible failure scenarios that may occur after the surgical procedure requiring screw insertion, as well as the characterization of fracture damage and estimation of mechanical responses under varying screws fixation angles [34, 35]. Thereby, the impact of screw configuration angular parameters in fracture pattern and stress distributions were investigated via computational model considering a stress-based criterion [36, 37]. In the study by [23], the mechanical behaviour of instrumented metastatic vertebra in presence of pedicle screws has been investigated.

Bone metastases are the spread of cancer cells from a primary tumour to the bones [38]. There are two main types of bone metastases: osteolytic and osteoblastic. Osteolytic bone metastases are caused by the destruction of normal bone tissue. This occurs when cancer cells produce substances that stimulate osteoclasts, the cells that break down bone. Osteoblastic bone metastases are caused by the deposition of new bone tissue. This occurs when cancer cells produce substances that stimulate osteoblasts, the cells that build bone. The findings of study [23, 39] showed that the prediction of mechanical properties has been affected by the size, location and nature of the metastasis. Moreover, it has been concluded that a metastasis situated near the screws produces a higher influence on fracture load response compared to a metastasis far from the screws. As a consequence, a finite element phase field model has been hereof implemented in order to validate numerically the existing outcomes in the literature resulting from the variation of the screws insertion angle in a human vertebra, with the aim of further developing a coupled model with two or more fused vertebrae. To reduce discrepancies between the current numerical implementation and the real one, spatially heterogeneous elastic properties and phase field parameters have been meticulously derived through a computational procedure based on the estimation of bone density properties. This process has enabled the characterization and modelling of elastic properties across spatial dimensions, along with the nuanced determination of phase field parameters, contributing to a more comprehensive understanding of the damaged vertebral body.

The paper is organized as follows: Sect. 2 provides the CAD models of the screws and the vertebra, which are discretized and have their material properties set. It also covers the virtual insertion of pedicle screws into the vertebra. Section 3 introduces the phase field finite element method

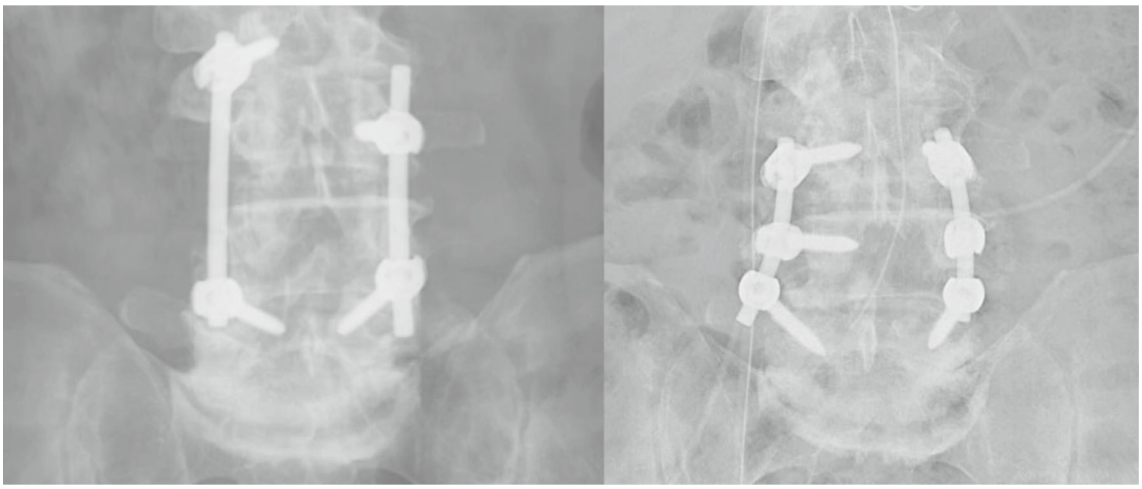

Fig. 1 The left image depicts the X-ray of the incorrect spinal stabilization procedure by the insertion of the pedicle screws in the vertebrae of the lumbar region, whereas the right image shows the X-ray of the re-intervention showing the correct spinal stabilization (image taken from [31])

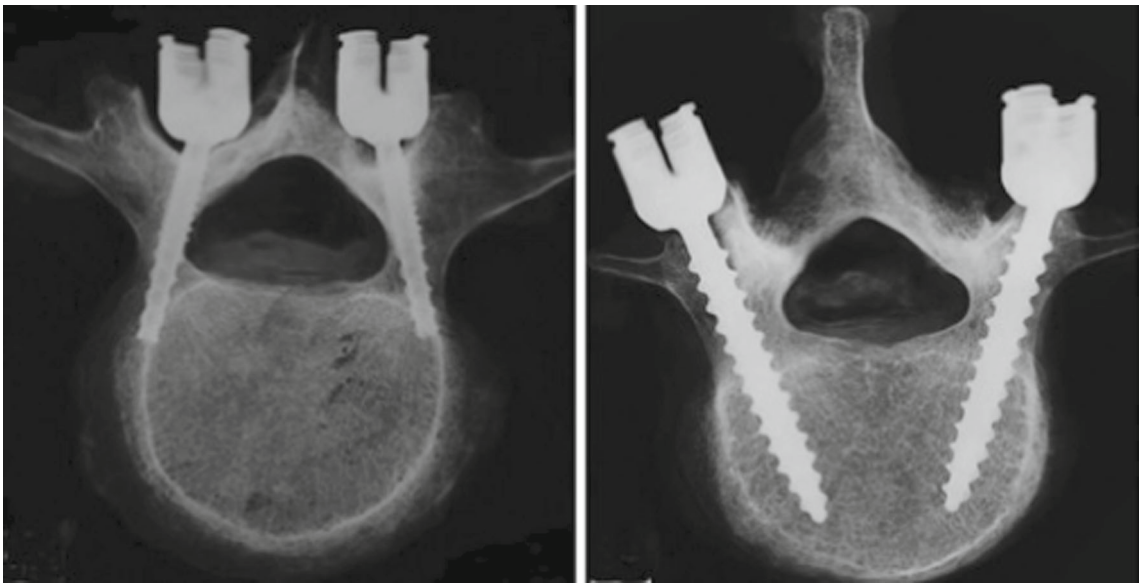

Fig. 2 Microradiographs showing different screw types and fixation trajectories. Cortical screw (left) and pedicle screw (right) placement (image taken from [30])

strategy implemented in this study. The staggered and monolithic phase field models are detailed in Sect. 4. Section 5 presents the boundary conditions and parameter setup for the numerical phase field method. Additionally, it includes a mesh sensitivity analysis of the phase field framework applied to several discretized models of vertebra-screws. Finally, Sect. 6 presents the main results in terms of damage patterns. It considers various screws insertion trajectories for different vertebral movements and presents a discussion comparing the outcomes with other relevant works in this field. Lastly, Sect. 7 characterizes the mechanical responses and fracture patterns of the vertebral body with the screws inserted in the presence of metastatic conditions, namely osteolytic and osteoblastic lesion types.

2 Human vertebra-pedicle screws finite element model

2.1 Models and materials

The L4 lumbar vertebra model was obtained from a Computer Tomography (CT) scan images from the spine of 49-year-old female patient of 62 Kg weight, as described in [34]. The solid cylindrical pedicle screws have length of 40 mm. The major and minor diameters of screws are 6.5 mm and 4.3 mm, respectively (please see [35] for additional details). The CAD models of the pedicle screws virtually inserted in the L4 vertebra are depicted in Fig. 3. The phase field model has been evaluated for three different screws fixation angles,

indicated by the vector $\vec{\alpha} = (\alpha_1, \alpha_2)$. Here, α_1 represents the insertion angle in the cranio-caudal (CC) direction, and α_2 indicates the insertion angle in the medio-lateral (ML) direction [34], as shown in Fig. 3a. In particular, the mesh sensitivity analysis is conducted using the screws insertion trajectory combination $\vec{\alpha} = (-5, 0)$, which means that the screws are fixed with a negative angle of $-5°$ in the CC direction and a neutral angle of $0°$ in the ML direction.

To import the combined vertebra-screws CAD model into the finite element environment `FEniCS` [40], uniform tetrahedral meshes are constructed. This is achieved by transferring the assembled STL model's triangular mesh into the pre-processing software HyperMesh [41], which generates the required tetrahedral solid. The solid is then assessed and converted into a MSH file using the Gmsh platform [42]. Multiple refined meshes have been created, ranging from 60 thousand elements to 700 thousand elements. Please refer to Fig. 3b for visualization of these meshes.

Bone density properties have been considered for the material of the L4 vertebra using CT data [43–45]. In this regard, a constant Poisson's ratio of $\nu = 0.3$ was assumed, and isotropic and linear elastic material properties were adopted with a heterogeneous distribution of the Young's modulus E obtained from the interpolation of the spatial distribution of the material properties from the CT data of the vertebra [34, 35]. Such distribution differentiates the cortical bone from the trabecular bone. For trabecular bone, an elastic modulus ranging between 0.4 and 3 GPa was derived, while for cortical bone, the range was between 12 and 14 GPa, as shown in Fig. 4a. In what regards to the pedicle screws, surgical procedures commonly use biomedical implants or replacements made of the titanium alloy Ti-6Al-4V [46, 47]. Therefore, the chosen mechanical properties for the pedicle screws are a Young's modulus of 110 GPa (Fig. 4b) and a Poisson's ratio of 0.4, as in [34, 48].

3 Phase-field approaches to fracture with spectral decomposition

With reference to an arbitrary body occupying a domain $\Omega \in \mathbb{R}^{n_{dim}}$, with boundary $\partial\Omega \in \mathbb{R}^{n_{dim}-1}$, in the Euclidean space of dimension n_{dim}, in which an evolving internal discontinuity Γ is postulated to exist, a material point is denoted by $\mathbf{x}$ and body forces by $\mathbf{b} : \Omega \to \mathbb{R}^{n_{dim}}$. Mixed conditions are prescribed along non-overlapping Neumann and Dirichlet regions of the boundary $\partial\Omega_N \cup \partial\Omega_D = \partial\Omega$ in the usual form

$$\mathbf{u} = \overline{\mathbf{u}} \quad \text{on } \partial\Omega_D \quad \text{and} \quad \boldsymbol{\sigma} \cdot \mathbf{n} = \overline{\mathbf{T}} \quad \text{on } \partial\Omega_N \tag{1}$$

where $\mathbf{n}$ denotes the outward unit normal to the boundary, $\mathbf{u}$ is the displacement field and $\boldsymbol{\sigma}$ is the Cauchy stress tensor, while $\overline{\mathbf{u}}$ and $\overline{\mathbf{T}}$ are prescribed surface displacements and tractions.

3.1 The regularized variational formulation

Within the regularized framework of the phase field approach [12, 20, 49, 50], the potential energy of the system can be decomposed into two terms as following

$$\Pi(\mathbf{u}, s) = \int_\Omega \psi^e(\boldsymbol{\varepsilon}, s)\, \mathrm{d}\mathbf{x} + \int_\Omega \mathcal{G}_c \gamma(s, \nabla s)\, \mathrm{d}\mathbf{x} \tag{2}$$

where $\psi^e(\boldsymbol{\varepsilon}, s)$ is the energy density of the bulk, now function of the damaged parameter s, and $\gamma(s, \nabla s)$ is the crack density functional, with ∇ denoting the spatial gradient operator. As a result, the total free energy density of the bulk $\hat{\psi}$ reads as

$$\hat{\psi}(\boldsymbol{\varepsilon}, s) = \psi^e(\boldsymbol{\varepsilon}, s) + \mathcal{G}_c \gamma(s, \nabla s).$$

The functional $\gamma(s, \nabla s)$ is assumed to be a convex function of s and its gradient ∇s and can be written, in agreement with the following expressions characterizing the AT2 model, as

$$\gamma(s, \nabla s) = \frac{1}{2}\left(\frac{s^2}{l_0} + l_0 |\nabla s|^2\right), \tag{3}$$

where l_0 stands for a regularisation characteristic length that can be related to the Young's modulus, the fracture toughness, and the tensile strength of the material, as specified in Sect. 5. To avoid the development of damage in compression, so to allow fracture growth only under tensile stress states, the following 'tensile/compressive' decomposition is herein assumed for the energy density in the bulk $\psi^e(\boldsymbol{\varepsilon}, s)$ [20, 51–54] and included in the formulation:

$$\psi^e(\boldsymbol{\varepsilon}, s) = g(s)\psi^e_+(\boldsymbol{\varepsilon}) + \psi^e_-(\boldsymbol{\varepsilon}), \tag{4}$$

where $g(s)$ is a damage function that is assumed in the simple form $g(s) = (1 - s)^2 + k$, where k is a residual stiffness (introduced to avoid ill-conditioning) and the positive and negative parts of the energy density are defined as

$$\psi^e_\pm(\boldsymbol{\varepsilon}) = \frac{\lambda}{2}\langle \pm \mathrm{tr}\boldsymbol{\varepsilon}\rangle^2 + \mu \mathrm{tr}\,(\boldsymbol{\varepsilon}_\pm)^2, \tag{5}$$

where λ and μ are the Lamé constants, $\mathrm{tr}(\cdot)$ denotes the trace operator and the positive and negative parts of the strain $\boldsymbol{\varepsilon}_\pm$ are defined as follows. With reference to the spectral representation for the strain (with eigenvalues ϵ_i and unit

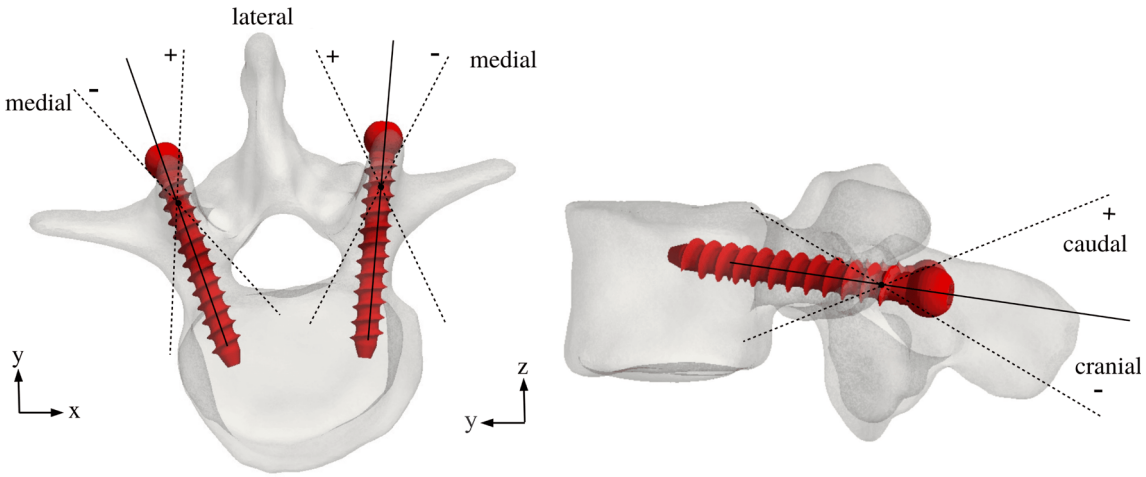

(a) Identification of CC and ML directions of the pedicle screws virtually inserted.

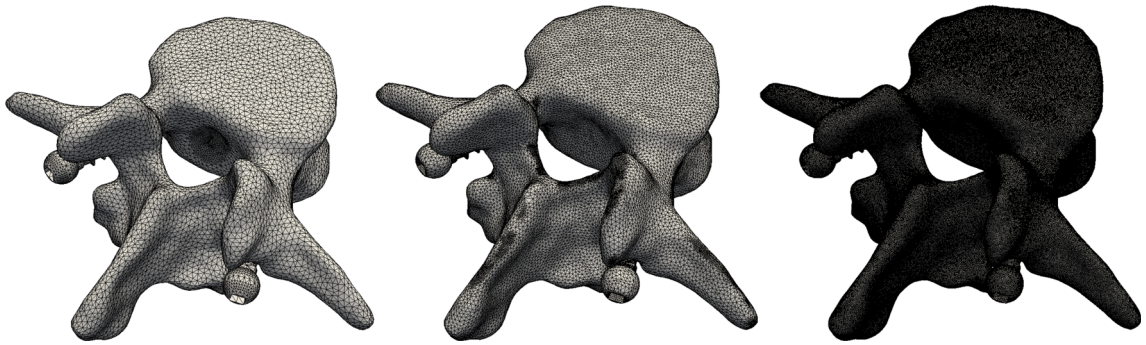

(b) Uniform computational discretized vertebra-screws meshes. From left to right: 100 Dof, 350 Dof, 700 Dof.

Fig. 3 CAD-based finite element of the vertebra-screws model

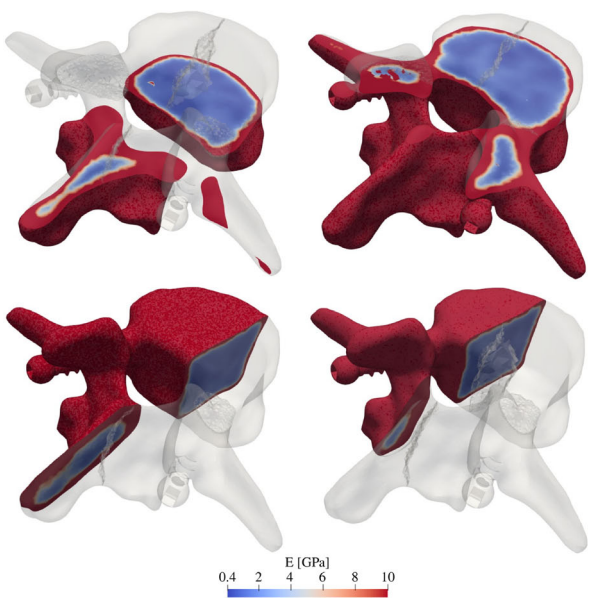

(a) Young's modulus (GPa) distribution of the vertebra. The red color represents the high stiffness layer given by the cortical bone, while the blue color indicates low stiffness layer given by the trabecular bone.

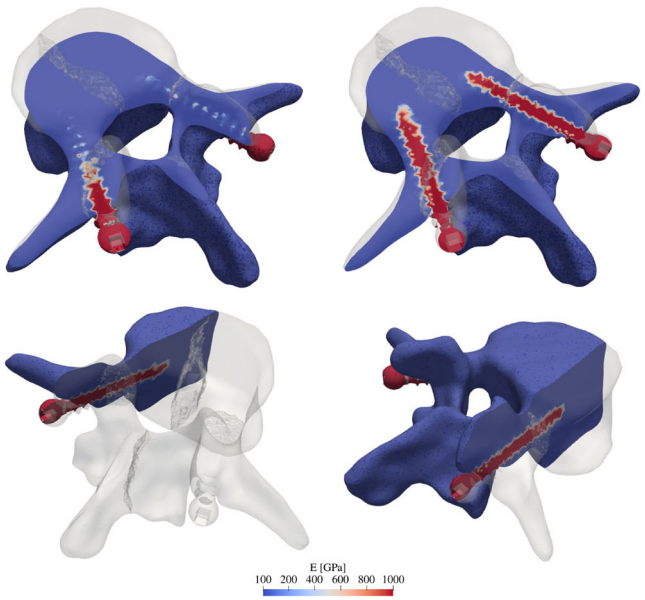

(b) Young's modulus (GPa) distribution of the pedicle screws. The red color illustrates the high stiffness assumed for the pedicle screws.

Fig. 4 Interpolated Young's modulus (GPa) distribution of the model vertebra-screws. For details of the distribution in (**a**), please see [34, 35]

eigenvectors $\boldsymbol{e}_i$), denoted as

$$\boldsymbol{\varepsilon} = \sum_{i=1}^{3} \epsilon_i \boldsymbol{e}_i \otimes \boldsymbol{e}_i, \tag{6}$$

the strain is additively decomposed as $\boldsymbol{\varepsilon} = \boldsymbol{\varepsilon}_+ + \boldsymbol{\varepsilon}_-$, so that the tensile and compressive parts associated to $\boldsymbol{\varepsilon}$ are

$$\boldsymbol{\varepsilon}_+ = \sum_{i=1}^{3} \langle \epsilon_i \rangle \boldsymbol{e}_i \otimes \boldsymbol{e}_i, \qquad \text{and} \qquad \boldsymbol{\varepsilon}_- = -\sum_{i=1}^{3} \langle -\epsilon_i \rangle \boldsymbol{e}_i \otimes \boldsymbol{e}_i, \tag{7}$$

respectively, where the Macaulay bracket operator is defined for every scalar x as $\langle x \rangle = (x + |x|)/2$.
A standard derivation [55] leads Eq. (5) to the Cauchy stress tensor from the strain energy density:

$$\begin{aligned} \boldsymbol{\sigma} &= g(s)\boldsymbol{\sigma}_+ + \boldsymbol{\sigma}_- = \{(1-s)^2 + k\}\,(\lambda \mathrm{tr}\boldsymbol{\varepsilon}_+ \mathbf{I} + 2\mu\boldsymbol{\varepsilon}_+) \\ &\quad + \lambda \mathrm{tr}\boldsymbol{\varepsilon}_- \mathbf{I} + 2\mu\boldsymbol{\varepsilon}_-, \end{aligned} \tag{8}$$

where $\mathbf{I}$ denotes the second-order identity tensor. The thermodynamic consistency of the above constitutive theory, in agreement with the Clausius-Duhem inequality, has been addressed in [20].

3.2 Weak form of the variational problem

The weak form corresponding to the phase field model for brittle fracture can be derived following a standard Galerkin procedure. In particular, the weak form of the coupled displacement and phase field damage problem according to Eq. (2) is:

$$\begin{aligned} \delta\Pi = &\int_\Omega \boldsymbol{\sigma}(\mathbf{u}) : \boldsymbol{\varepsilon}(\mathbf{v})\, \mathrm{d}\mathbf{x} - \int_\Omega 2\psi_+^e(\boldsymbol{\varepsilon})(1-s)\phi\, \mathrm{d}\mathbf{x} \\ &+ \int_\Omega \mathcal{G}_c \left\{ \frac{1}{l_0} s\phi + l_0 \nabla s \cdot \nabla \phi \right\} \mathrm{d}\mathbf{x} + \delta\Pi_{\mathrm{ext}}\,, \end{aligned} \tag{9}$$

where $\mathbf{v}$ is the vector of the displacement test functions defined on $\mathbf{H}_0^1(\Omega)$, ϕ stands for the phase field test function defined on $\mathrm{H}_0^1(\Omega)$. Equation (9) holds for every test functions $\mathbf{v}$ and ϕ. The external contribution to the variation of the bulk functional in Eq. (9) is defined as follows:

$$\delta\Pi_{\mathrm{ext}}(\mathbf{u}, \mathbf{v}) = \int_{\partial\Omega} \overline{\mathbf{T}} \cdot \mathbf{v}\, \mathrm{d}\Gamma + \int_\Omega \mathbf{b} \cdot \mathbf{v}\, \mathrm{d}\mathbf{x}. \tag{10}$$

4 Numerical FE schemes

4.1 Staggered solution scheme

The mechanical problem can be stated as: given the prescribed loading condition $\overline{\mathbf{u}}_n$ and $\overline{\mathbf{T}}_n$ at step n, find $\mathbf{u} \in \mathbf{U} = \left\{ \mathbf{u} \,|\, \mathbf{u} = \overline{\mathbf{u}}_n \text{ on } \partial\Omega_u, \mathbf{u} \in \mathbf{H}^1(\Omega) \right\}$ such that

$$\begin{aligned} \mathcal{E}_{\mathbf{u}}(\mathbf{u}, s; \mathbf{v}) := &\int_\Omega \boldsymbol{\sigma}(\mathbf{u}) : \boldsymbol{\varepsilon}(\mathbf{v})\, \mathrm{d}\mathbf{x} - \int_{\partial\Omega} \overline{\mathbf{T}}_n \cdot \mathbf{v}\, \mathrm{d}\Gamma \\ &- \int_\Omega \mathbf{b} \cdot \mathbf{v}\, \mathrm{d}\mathbf{x} = 0, \ \forall \mathbf{v} \in \mathbf{H}_0^1(\Omega), \end{aligned} \tag{11}$$

while the phase field problem is formulated as: find $s \in S = \left\{ s \,|\, s = 1 \text{ on } \Gamma, s \in \mathrm{H}^1(\Omega) \right\}$ such that $\forall \phi \in \mathrm{H}_0^1(\Omega)$:

$$\begin{aligned} \mathcal{E}_s(\mathbf{u}, s; \phi) \ := &\int_\Omega \mathcal{G}_c\, l_0\, \nabla s \cdot \nabla \phi\, \mathrm{d}\mathbf{x} \\ &+ \int_\Omega \left(\frac{\mathcal{G}_c}{l_0} + 2H \right) s\phi\, \mathrm{d}\mathbf{x} - \int_\Omega 2H\phi\, \mathrm{d}\mathbf{x} = 0\,, \end{aligned} \tag{12}$$

where $H(\boldsymbol{\varepsilon}) = \max_{\tau \in [0,t]} \left\{ \psi_+^e(\boldsymbol{\varepsilon}(\tau)) \right\}$ is the strain history function, accounting for the irreversibility of crack formation [17, 20].

To solve the quasi-static evolution problems for brittle fracture, isoparametric linear triangular finite elements are used for the spatial discretization, and a staggered solution scheme is considered. Staggered schemes based on alternate minimization exploit the convexity of the energy functional with respect to each individual variable $\mathbf{u}$ and s [56]. Here, an *ad hoc* developed solver has been implemented in the software `FEniCS`, see Alg. 1 for the staggered algorithm description. A series of benchmark tests taken from [20, 57] has been carried out to validate the methodology.

4.2 Newton–Raphson procedure

Even if the mechanical problem has been split into Eqs. (11) and (12), so that the phase field is reduced to a linear problem, non-linearity still remains, because of the piece-wise linearity of the constitutive law, which includes a spectral decomposition of the strain. Therefore, a consistent linearization is required, so that the linear form defined by the residual can be written as:

$$\begin{aligned} F_{\mathbf{u}}(\mathbf{u}, s; \mathbf{v}) = &\int_\Omega \Big\{ ((1-s)^2 + k)\boldsymbol{\sigma}_+(\mathbf{u}) : \boldsymbol{\varepsilon}(\mathbf{v}) \\ &+ \boldsymbol{\sigma}_-(\mathbf{u}) : \boldsymbol{\varepsilon}(\mathbf{v}) \Big\}\, \mathrm{d}\mathbf{x} - \int_{\partial\Omega} \overline{\mathbf{T}} \cdot \mathbf{v}\, \mathrm{d}\Gamma \\ &- \int_\Omega \mathbf{b} \cdot \mathbf{v}\, \mathrm{d}\mathbf{x}. \end{aligned} \tag{13}$$

Given $\mathbf{u}^k$ the current Newton–Raphson approximate solution at iteration k, the correction $\delta\mathbf{u}$ is therefore the solution

of the following linear variational problem: find $\delta\mathbf{u} \in \mathbf{U}_0 = \{\mathbf{u} \,|\, \mathbf{u} = \mathbf{0} \text{ on } \partial\Omega_u, \mathbf{u} \in \mathbf{H}^1(\Omega)\}$ such that $J_{\mathbf{u}}(\delta\mathbf{u}, \mathbf{u}^k, s; \mathbf{v}) = -F_{\mathbf{u}}(\mathbf{u}^k, s; \mathbf{v}), \quad \forall \mathbf{v} \in \mathbf{H}_0^1(\Omega)$ and then iterate as $\mathbf{u}^{k+1} = \mathbf{u}^k + \delta\mathbf{u}$. The Jacobian entering the formulation is

$$J_{\mathbf{u}}(\delta\mathbf{u}, \mathbf{u}, s; \mathbf{v}) = \int_\Omega \Big\{((1-s)^2 + k)\partial\boldsymbol{\sigma}_+(\delta\mathbf{u}, \mathbf{u}) : \boldsymbol{\varepsilon}(\mathbf{v}) + \partial\boldsymbol{\sigma}_-(\delta\mathbf{u}, \mathbf{u}) : \boldsymbol{\varepsilon}(\mathbf{v})\Big\}\, \mathrm{d}\mathbf{x}\,; \tag{14}$$

for details about the terms $\partial\boldsymbol{\sigma}_-$, $\partial\boldsymbol{\sigma}_+$, please see [18].

Algorithm 1 Staggered iterative scheme for phase field fracture at a step $n \geq 1$

1: **Input:** Displacements and phase field $(\mathbf{u}_{n-1}, s_{n-1})$ and prescribed loads $(\overline{\mathbf{u}}_n, \overline{\mathbf{T}}_n)$:
2: Initialize $(\mathbf{u}^0, s^0) := (\mathbf{u}_{n-1}, s_{n-1})$;
3: **for** $k \geq 1$ staggered iteration **do**:
4: Given s^{k-1}, solve the mechanical problem (13): $\mathcal{E}_{\mathbf{u}}(\mathbf{u}, s^{k-1}; \mathbf{v}) = 0$ for $\mathbf{u}$, set $\mathbf{u} := \mathbf{u}^k$;
5: Given $\mathbf{u}^k$, solve the phase field problem (14): $\mathcal{E}_s(\mathbf{u}^k, s; \phi) = 0$ for s, set $s := s^k$;
6: **if** $\max\{||\mathbf{u}^k - \mathbf{u}^{k-1}||/||\mathbf{u}^k||, |s^k - s^{k-1}|/|s^k|\} <$ tol: **then**
7: set $(\mathbf{u}^k, s^k) := (\mathbf{u}_n, s_n)$;
8: **else** $k + 1 \to k$.
9: **end if**
10: **end for**
11: **Output:** $(\mathbf{u}_n, s_n)$.

At this stage, it is fundamental to remark that, in order to predict crack trajectories in human vertebrae under tensile/compressive stress states, the phase field finite element method will be formulated. This formulation involves decomposing the strain energy density $\psi^e(\mathbf{u}, s)$ in Eq. (4) based on spectral diagonalization, as described in [20], into active and passive parts. This decomposition allows for the application of material response degradation only in tension. The variational formulation is then implemented in the `FEniCS` environment, utilizing the MPI (message passing interface) parallelization library, which accelerates the computational time.

4.3 Monolithic solution scheme

A monolithic solver has also been implemented in `FEniCS`. The tangent operator of the non-linear variational functional given by:

$$\begin{aligned}\mathcal{E}_{\mathbf{u},s}(\mathbf{u}, s; \mathbf{v}, \phi) := &\int_\Omega \boldsymbol{\sigma}(\mathbf{u}) : \boldsymbol{\varepsilon}(\mathbf{v})\, \mathrm{d}\mathbf{x} \\ &- \int_\Omega 2H(\boldsymbol{\varepsilon})(1-s)\phi\, \mathrm{d}\mathbf{x} \\ &+ \int_\Omega \mathcal{G}_c \left\{\frac{1}{l_0} s\phi + l_0 \nabla s \cdot \nabla\phi\right\} \mathrm{d}\mathbf{x} \\ &+ \int_{\partial\Omega} \overline{\mathbf{T}} \cdot \mathbf{v}\, \mathrm{d}\Gamma + \int_\Omega \mathbf{b} \cdot \mathbf{v}\, \mathrm{d}\mathbf{x},\end{aligned} \tag{15}$$

is computed via the symbolic derivative `derivative`, the monolithic algorithm scheme can be visualized in Alg. 2.

Algorithm 2 Monolithic iterative scheme for phase field fracture at a step $n \geq 1$

1: **Input:** Displacements and phase field $(\mathbf{u}_{n-1}, s_{n-1})$ and prescribed loads $(\overline{\mathbf{u}}_n, \overline{\mathbf{T}}_n)$:
2: Solve the coupled non-linear variational problem via Newton-Raphson iterative scheme:
3: $\mathcal{E}_{\mathbf{u},s}(\mathbf{u}_n, s_n; \mathbf{v}, \phi) = 0, \quad \forall (\mathbf{v}, \phi) \in \mathbf{H}_0^1(\Omega) \times \mathrm{H}_0^1(\Omega)$
4: **Output:** $(\mathbf{u}_n, s_n)$.

5 Phase field modelling to pedicle screws in human vertebra

5.1 Boundary conditions and numerical implementation

Although spine models have been extensively exploited and validated in the literature [58], the present finite element phase field method focuses on a single vertebral body, as observed in other studies [35, 59]. In this study, the loadings are addressed on the inserted screws in the L4 vertebra, which will be simultaneously constrained. Throughout all the numerical implementations, the boundary conditions were set to replicate the principal movements permitted by the vertebral column. For this purpose, the pedicle screws head have been loaded to reproduce flexion (bending forward) and extension (bending backwards) (green arrows in Fig. 5), rotation (torsion/twisting) (red arrows in Fig. 5). The centre of the L4 vertebra has been assumed as the rotation axis centre for the twisting loading mode. Meanwhile, a compressive force of $F_v = 5$ N has been applied over the superior endplate surface of the vertebral body, while the inferior endplate has been constrained. Furthermore, the vertebral fracture patterns have been simulated by incrementally applying a quasi-static force to the screw heads for all the studied movements. Fundamentally, the total force applied at each loading step corresponds to 10% of the constant compressive load F_v.

The numerical phase field procedures were implemented in a high-performance computing (HPC) system, utilizing parallel computing and dividing the model into three smaller tasks. The computational time ranged from 2 h for the coarsest mesh to 30 h for the finest mesh. Six cores were utilized, with an average of 200 GB of RAM per core. It is worth mentioning that the extension and flexion loading modes required more time for simulation, necessitating the use of additional cores and computational memory to improve the efficiency of these movement modes.

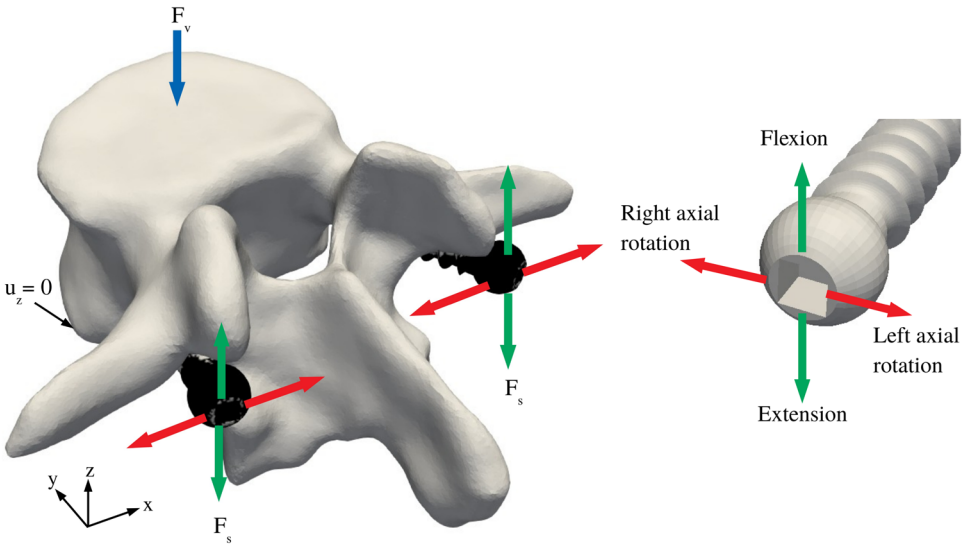

Fig. 5 Boundary conditions and loading regimes employed on the vertebra-screws models for numerical implementation

5.2 Parameters calibration and mesh sensitivity analysis

With the aim of achieving an appropriate mesh discretization for obtaining accurate numerical phase field responses for various physiological motions, a meticulous mesh sensitivity analysis has been conducted using the staggered scheme phase field finite element method reported in Alg. 1. The vertebra-screws mesh model has been uniformly discretized in tetrahedral elements at various refinement levels, ranging from 60k to 350k degrees of freedom (DoFs).

Prior to conduct the mesh sensitivity analysis, it must be recorded that the phase field parameters have to be delicately calibrated. The critical energy release rate $\mathcal{G}_c$ plays a crucial role in phase field modelling for bone application, where throughout experiments, different values of $\mathcal{G}_c$ have been obtained at different aged cortical bones [27, 60]. For those reasons, when a mesh sensitivity analysis is being conducted in a biological material, the phase field parameters must also be carefully examined. As such, a power-law equality is usually assumed (see [61]) by which the critical energy release rate $\mathcal{G}_c$ is derived from bone density properties, namely

$$\mathcal{G}_c = \mathcal{G}_{c,0}\left(\frac{E}{E_0}\right)^{\beta}, \tag{16}$$

where the parameters have been set as $E_0 = 20$ GPa, $\mathcal{G}_{c,0} = 0.01$ N/mm, and $\beta = 0.8$ are the base elastic modulus, the base critical energy release rate and the power-law exponent, respectively [36].

Through the implementation of the staggered phase field scheme Alg. 1, Fig. 6 presents the numerical analysis comparing the outcomes in the extension loading mode for different mesh refinements, with the screws insertion angle set as $\vec{\alpha} = (-5, 0)$. Fig. 6a depicts the load versus displacement curves juxtaposed, indicating that as the mesh becomes finer, the vertebra-screws model can bear more load. The error is defined as $100\% \times |F_{\max} - \hat{F}_{\max}|/|\hat{F}_{\max}|$, where $F_{\max}$ is the maximum peak load at the crack onset under extension loading for each simulation and $\hat{F}_{\max}$ is the mean maximum peak load at the crack onset under extension loading as reported in [34]. Figure 6b illustrates the relative error as the number of elements increases. According to [34], it can be noticed that mesh convergence is satisfactorily achieved at a relative error of less than 5%. Therefore, assuming a mesh size between 200k and 350k elements is acceptable for characterizing the fracture patterns in the simulated physiological movements. Nonetheless, in terms of characterizing the damage patterns, the present mesh sensitivity analysis revealed no significant distinctions among the different mesh refinements. Moreover, the computational cost aligns well with the numerical outcomes using a mesh with 200k elements. This is further supported by Fig. 6c, which displays the fractured volume as the loading step varies, and it can be noted that the curve of 200k elements deviates very little from the curve of 350k elements. The damaged volume was calculated at each loading step by considering the number of finite elements in which the phase field was in the interval $[0.9, 1]$, divided by the total number of elements of the mesh. Still, Fig. 7 delineates a comprehensive comparison of distinct mesh refinements, showcasing contour profiles of the phase field on a horizontal cut at the same loading step under extension mode motion. These convergence analyses demonstrate good agreement with previous studies [34, 35]. In terms of damage type, although the phase field model captured similar damage patterns for all mesh refinements, coarser meshes exhibited more rapid fracture spread within the cortical part.

The length scale l_0 parameter is deeply inserted for modelling phase field, considering that for a sufficiently small

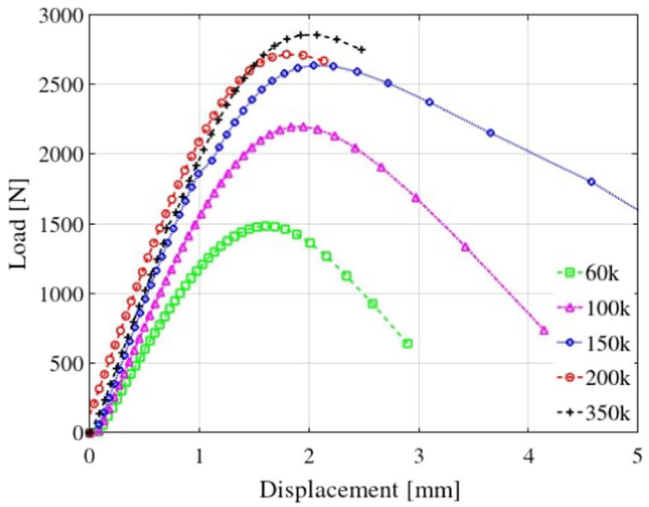

(a) Load vs. Displacement curves for different mesh refinements.

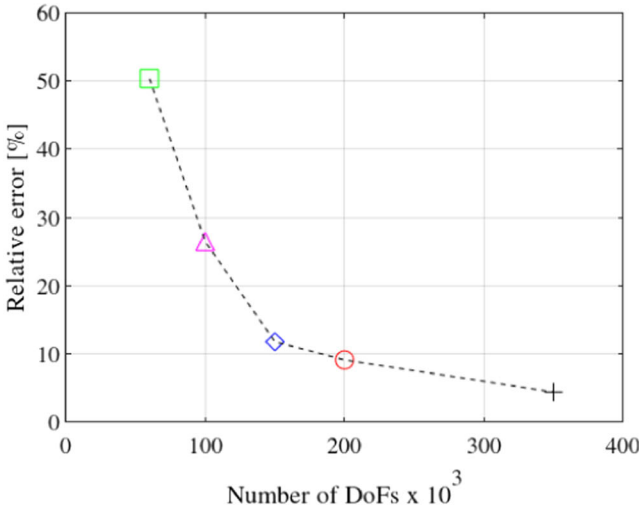

(b) Relative error as function of the number of degrees of freedom.

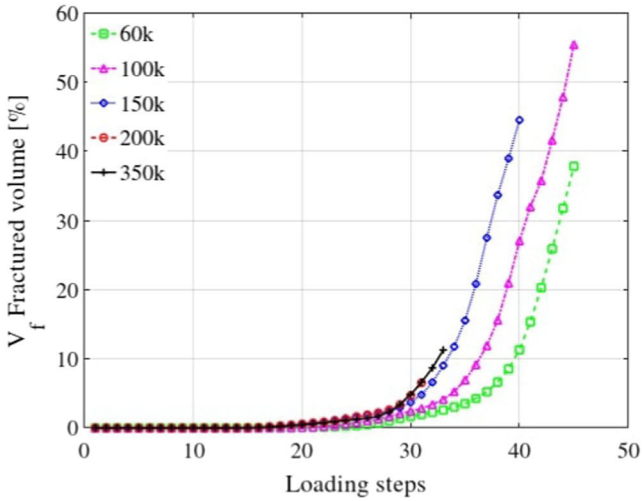

(c) Vertebral fractured volume as function of the loading steps for different mesh refinements.

Fig. 6 Mesh sensitivity analysis: Extension mode movement at screws fixation angle of $\vec{\alpha} = (-5, 0)$.

length scale l_0, the functional (9) converges to the total potential energy functional, in the sense that the global minimizers of Π_{l_0} will also converge to that of Π. This entails that the length scale must be carefully chosen, rather than setting it arbitrarily.

Having said that, on one hand, the characteristic length scale l_0 that smears the regularized crack can be obtained either from microscopic structural-related mechanisms [62, 63], and further derived from a formula combining the Young's modulus E, the critical energy release rate $\mathcal{G}_c$ and the maximum strength of the material at failure σ_{max} [64], as evidenced in several studies [65–67]. However, this relation is known to be valid just in the case of uniaxial tension of an one-dimensional bar and relies on the knowledge of σ_{max}, which is a difficult material parameter to be found in literature.

On the other hand, the characteristic length scale l_0 can be interpreted, and therefore calibrated, as a structural factor from bone properties [27, 61]. In particular, in a biological material, as cortical bone for instance, the length scale can be attributed to the lamellar microstructure, which may trap the crack tip within it, deflecting or stopping the leading edge of the crack [68]. Moreover, structural changes in cortical bone due to ageing affect crack path and damage properties [43, 60, 69]. In accordance with the estimations made in [61, 70], an examination of the role played by the characteristic length scale l_0 is also developed here.

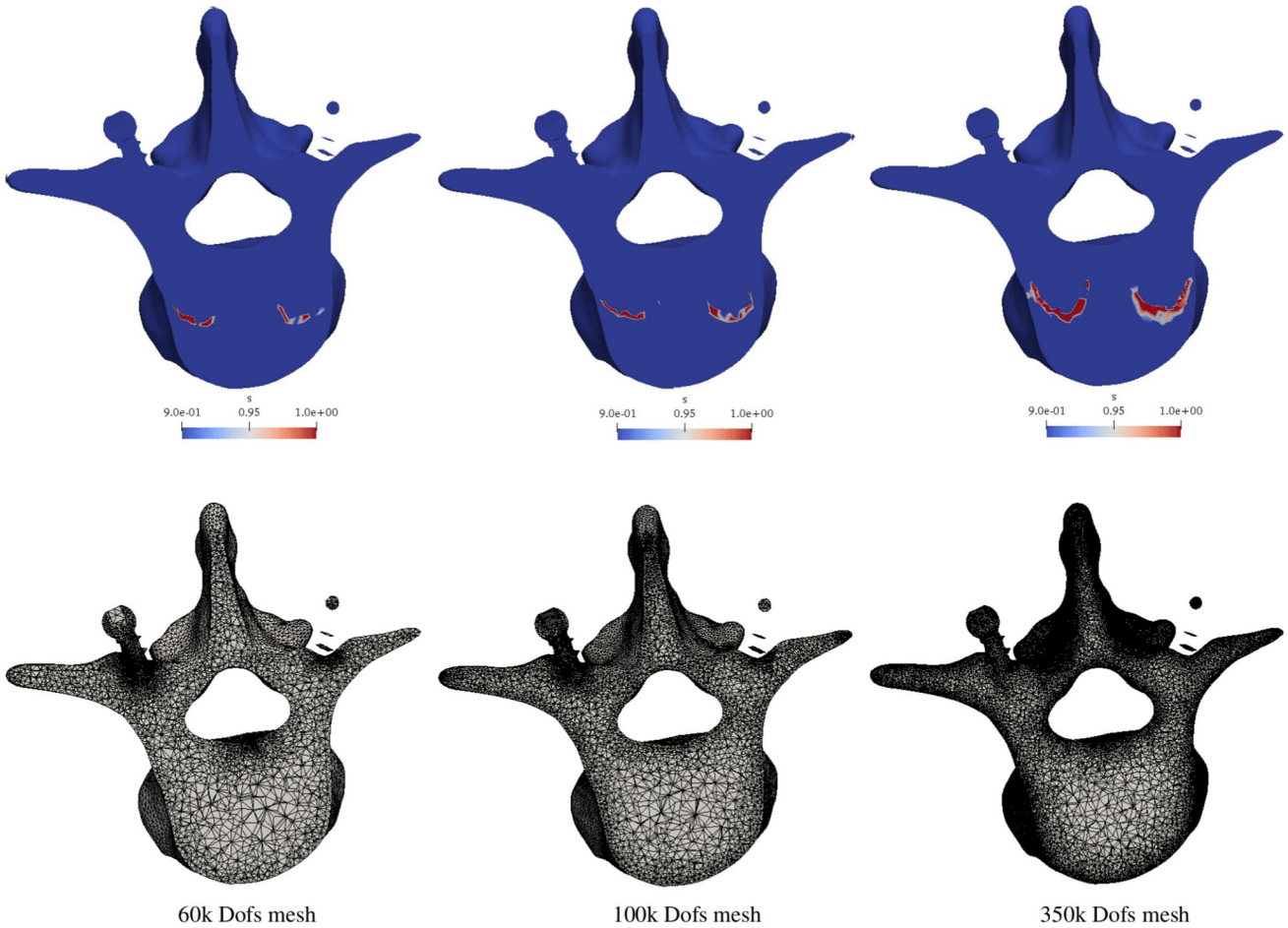

Fig. 7 Contour Profiles of the phase field variable for different mesh refinements at the same cutting plane and the same loading step

To address the problem of calibrating l_0, a series of simulations have been conducted varying $l_0 \in \{5 \cdot 10^{-5}, 10^{-4}, 5 \cdot 10^{-4}\}$ mm and the value of $l_0 = 10^{-4}$ mm has been selected to be the one that provides the closest value of the peak load in extension ($F_{\max} = 2715$ N)(refer to Fig. 8) compared to the value reported in the literature [23], corresponding to $F_{\max} = 2929$ N, corresponding to a relative error of 4.45%. As mentioned in the previous section, from a biomechanical standpoint, the characteristic fracture length scale l_0 can be associated with the typical size of bone microstructure, i.e., osteon ($10 \div 500\,\mu$m), lamellae ($3 \div 7\,\mu$m), and collagen fibril ($0.5\,\mu$m). In these regards, image-based identification procedures would be necessary to characterize the most critical scale involved in fracture phenomena.

Taking into consideration the previous mesh sensitivity analysis, with a mesh of 200k elements, a screws insertion angle of $\vec{\alpha} = (-5, 0)$ in extension mode motion, Fig. 8 indicates that the apparent peak load from the phase field scheme increases as the characteristic length scale l_0 is reduced, as expected based on previous results reported in the literature [71, 72].

5.3 Staggered versus monolithic numerical schemes

A numerical comparison has been conducted to assess the performances of both the staggered and monolithic numerical schemes, as described in Sects. 4.1 and 4.3, respectively, in terms of their accuracy in reproducing the damage evolution patterns and the load versus displacement curves. The outcomes of these campaigns are depicted in Fig. 9. For this comparative analysis, the discretized vertebra-screws model consisting of 300k elements has been considered, with the screws inserted at an angle combination of $\vec{\alpha} = (-5, 0)$, in a counter-clockwise torsion motion.

In terms of accuracy, the load versus displacement curves, presented in Fig. 9a, are more accurate in the monolithic scheme due to the fact that the binding reaction on the vertebra endplate is zero and deviates very little. Furthermore, the fractioned volume outcomes are similar for both approaches, as Fig. 9b displays. It can also be pointed out that, the damage pattern obtained from the monolithic method bears resemblance to the evolution of the damage observed in the staggered simulation, see Fig. 9c. Nevertheless, con-

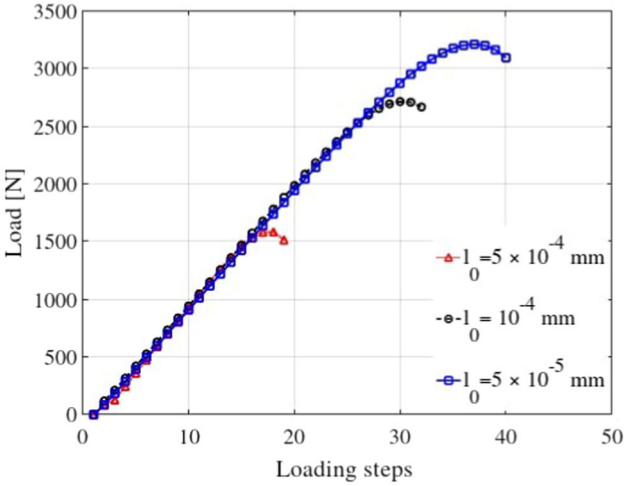

Fig. 8 Load versus loading steps obtained for different values of the length scale parameter l_0. Extension mode movement at screws fixation angle of $\vec{\alpha} = (-5, 0)$.

sidering the computational time consumed, the advantages of using the staggered scheme outweigh the potential benefits offered by the monolithic technique. While the staggered simulation took approximately 3.5 h to be completed, the monolithic running time exceeded 15 h.

6 Computational analysis

6.1 Characterization of loading modes

Continuing with the comparative investigation of the various screw insertion angles, namely $\vec{\alpha} = (-5, 0)$, $\vec{\alpha} = (-5, -5)$, and $\vec{\alpha} = (+5, +5)$, Fig. 10 highlights how the screw configuration influences the mechanical responses of the vertebral body in different motion regimes. The load versus displacement curves generated from the phase field finite element method are displayed in Figs. 10a–c, representing the vertebral movements of extension, flexion, and torsion, respectively. In these three cases analysed, the load has been computed as the vincular reaction on the bottom of the vertebra. In the cases of extension and flexion modes, it can be seen a linear elastic phase, followed by a softening due to the occurrence of fracture inside the vertebra, whereas in the case of rotation movement, the vincular reaction on the bottom is equal to zero, until a critical angle is reached and the fracture is activated.

Regarding the damage patterns, the counter-clockwise torsion motions simulated for the insertion angles $\vec{\alpha} = (-5, 0)$, $\vec{\alpha} = (-5, -5)$, and $\vec{\alpha} = (+5, +5)$ were characterized by the formation of asymmetric damage, where the damage occurrence is more prominent on the side that experiences greater loading as the steps increase. Additionally, in terms of extension and flexion regimes, symmetrical patterns were observed for all three screw fixation angle combinations, as expected. The characterizations presented demonstrate the effectiveness of the current phase field modelling as a robust tool for capturing damage and delineating mechanical aspects in biological tissues. Moreover, they also demonstrate good agreement with recent works found in the literature [34, 35]. To achieve a precise estimation of sharp fracture, it is necessary to employ mesh elements with a size, denoted as h, considerably smaller than the characteristic length scale l_0 [12, 19]. However, in the current investigation, the phase field model serves the dual purpose of representing damage, encompassing more than just a sharp fracture pattern. Consequently, the assumed value of l_0 in the numerical campaign suits and effectively characterizes the damage induced by the pedicle screws within the vertebra model, as visually demonstrated in Fig. 11, and which can be satisfactory contrasted to the evolution of the damage patterns from Fig. 9 in [35], showing that the present phase field model accurately captures the evolution of the damage within the vertebral body. Figure 11a, b show a symmetrical trend regarding the evolution of the damage caused by the screws on extension and flexion movements, respectively. On the contrary, the counter-clockwise rotation regime is characterised by an asymmetrical evolution of the damage, as demonstrated in Fig. 11c.

7 Osteolytic and osteoblastic metastatic lesion models

In this section the damage patterns within the vertebra-screws model are assessed and characterised in the presence of metastatic lesions by applying the phase field method. The metastasis lesion types considered for the simulations are osteolytic and osteoblastic. Both metastatic tissues have been modelled following the material properties which accounts for the interaction bone-metastasis as in [23, 39]. Figure 12 illustrates the spherical metastatic lesions within the vertebral domain, centred at a material point (10, 20, 0), assuming radii of 5 mm (Fig. 12a) and 10 mm (Fig. 12b).

Figure 13 shows the altered Young's modulus E, for the metastatic vertebrae, which have been calibrated by considering a weakening effect following Gaussian-like distributions centred at the centre of the spherical lesions at material point (10, 20, 0) and radii of 5 mm and 10 mm [23]. In the case of an osteolytic lesion, the Gaussian-like distribution was chosen such as a local softening could be induced, as depicted in Fig. 13a, b, whereas in the case of an osteoblastic metastasis, the Gaussian-like distribution adopted creates a local stiffening, seen in Figs. 13c, d. Likewise, the critical energy release rate $\mathcal{G}_c$ for both metastatic lesions have been derived following the relation stated in Eq. (16).

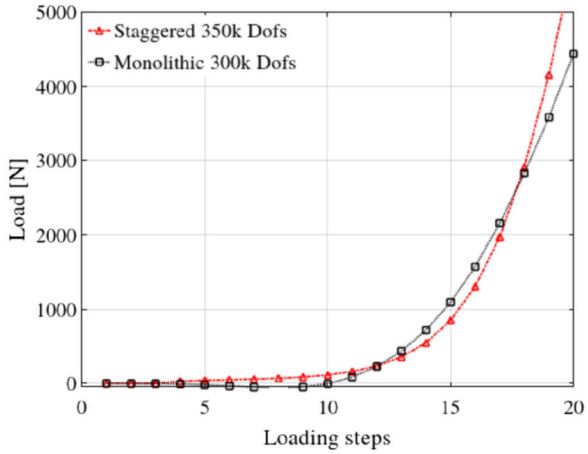

(a) Applied loading on a counter-clockwise axial rotation loading regime applied on the head of the screws as function of the loading step.

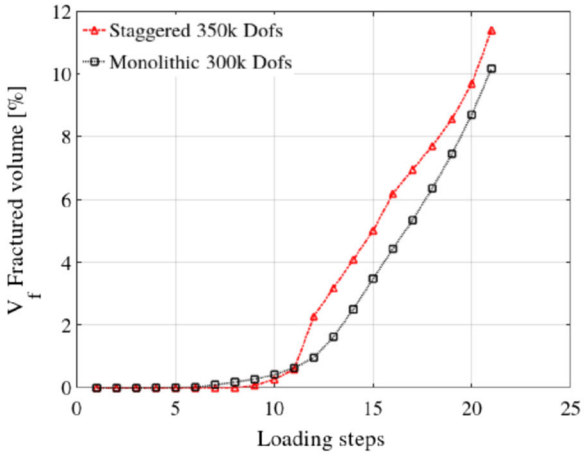

(b) Fractured volume of the vertebra on a counter-clockwise axial rotation loading regime applied on the head of the screws as the loading step increases.

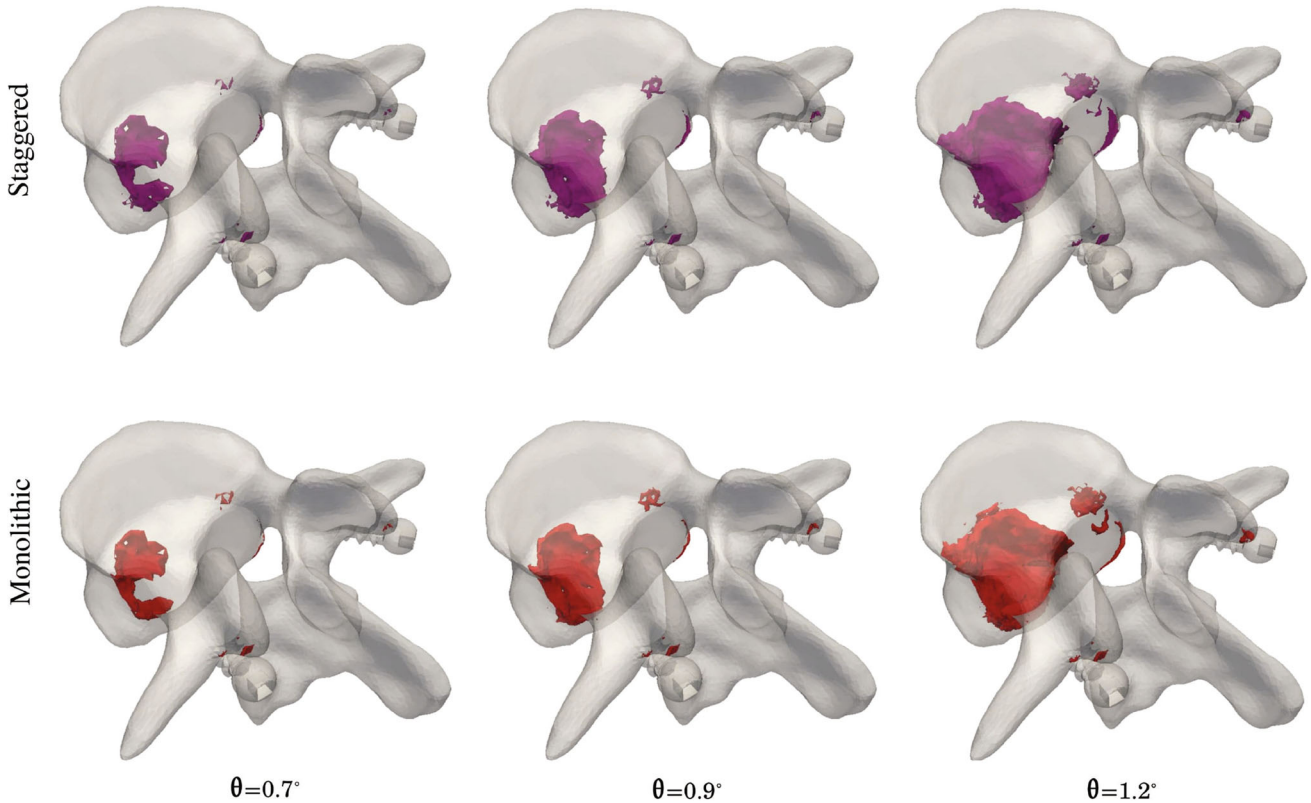

(c) Damage pattern comparisons between staggered and monolithic phase field models on a counter-clockwise axial rotation regime.

Fig. 9 Staggered and monolithic phase field models contrasted on a counter-clockwise axial rotation regime

The mechanical responses have been derived by applying the phase field model to the aforementioned metastatic lesions under the vertebral movement of vertical extension. Figure 14 shows the load versus displacement charts from the osteolytic metastasis performances, see Fig. 14a, and from the osteoblastic lesion simulations, see Fig. 14b. Overall, the vertebrae within an osteoblastic are characterized by higher load peaks in contrast to the vertebrae within the effect of an osteolytic metastasis. Moreover, the curve for the osteoblastic lesion of radius 10 mm is characterized by a higher stiffness than the osteolytic lesion of radius 10 mm. However, in the case of a lesion with a radius of 5 mm, the osteolytic model demonstrates a higher peak load value than the osteoblastic model. Those outcomes are in good matching with the find-

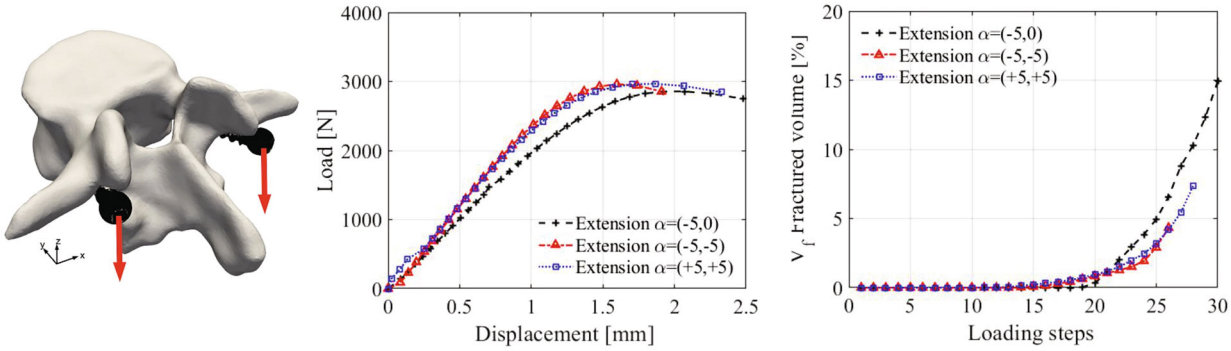

(a) Load vs. Displacement curves at extension mode motion.

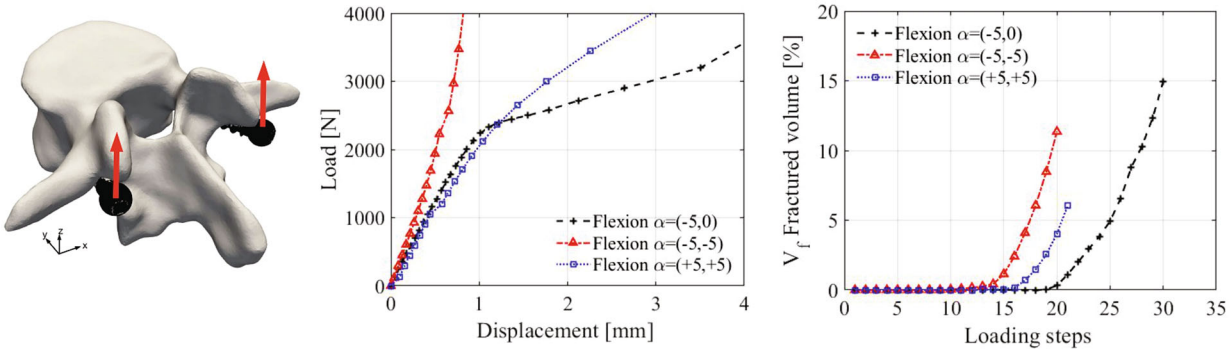

(b) Load vs. Displacement curves at flexion mode motion.

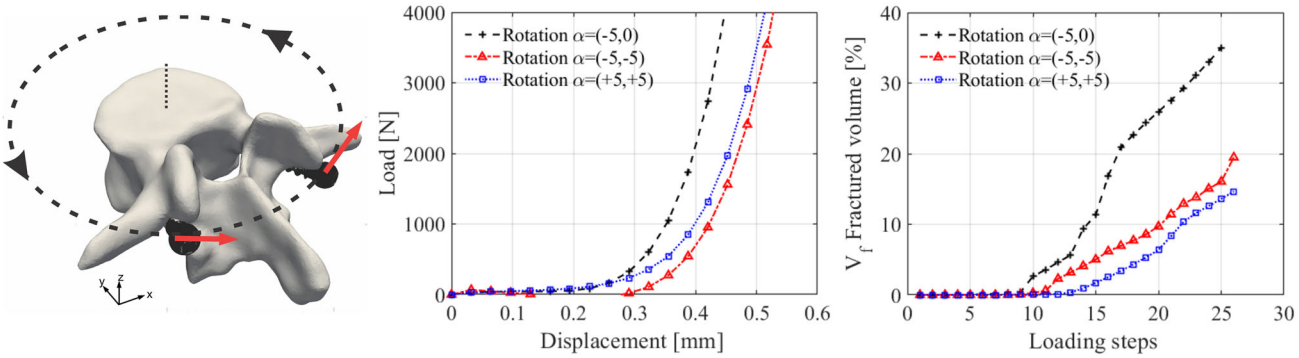

(c) Load vs. Displacement curves at torsion mode motion.

Fig. 10 Comparative analyses among the extension, flexion and torsion modes, at screws fixation angles of $\vec{\alpha} = (-5, 0)$, $\vec{\alpha} = (-5, -5)$ and $\vec{\alpha} = (+5, +5)$

ings in [23] considering the P2 position for the lesions (refer to Figs. 7(b),(d) and 10(h) in [23]). Accordingly, as the osteolytic lesions increases in size, the peak load reduces, this effect is well reported in [73], which states that as the region of the metastasis increases, the stiffness of the vertebral body reduces.

In terms of damage pattern, the influences of the induced osteoblastic spherical lesions having radii respectively of 5 mm and 10 mm are depicted in Fig. 15. It can be observed that, from Fig. 15a, it is worth adding that the damage pattern of the model vertebra-screws within the osteoblastic metastasis having radius of 5 mm resembles the fracture pattern of a no lesion vertebra, reported in Fig. 11b. On the other hand, the vertebra-screws model under the effect of a osteoblastic spherical lesion having radius of 10 mm significantly affect fracture characterization, demonstrating an asymmetric trend, in which the damage has spread more rapidly in the side where the metastasis is located, as seen in Fig. 15b.

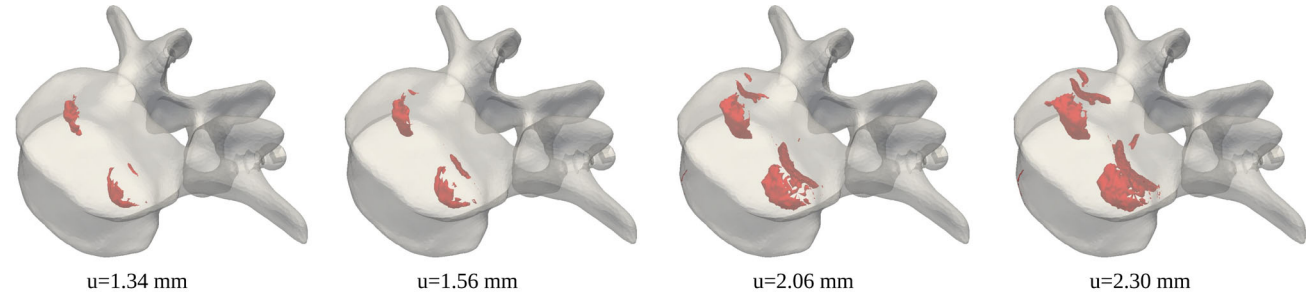

(a) Back view of the evolution of the fracture pattern under vertical extension loading.

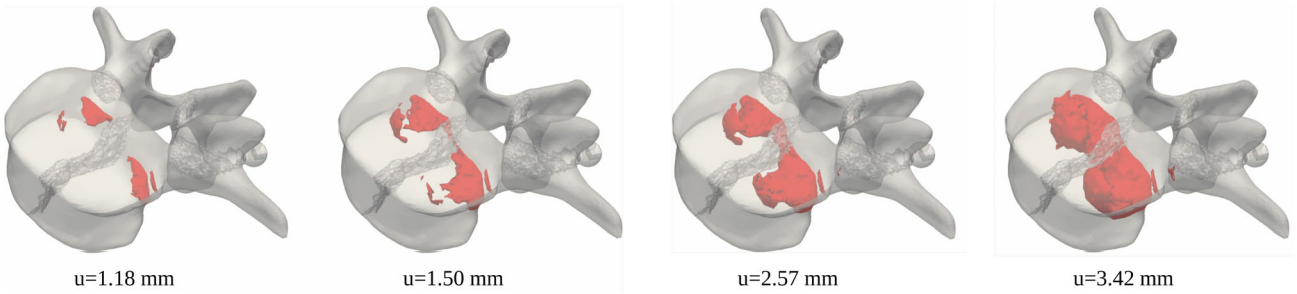

(b) Back view of the evolution of the fracture pattern under vertical flexion loading regime.

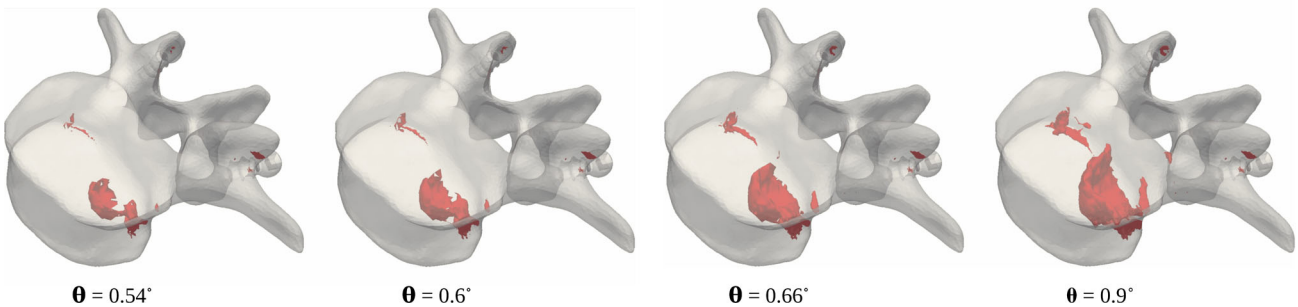

(c) Back view of the evolution of the fracture pattern under a counter-clockwise axial rotation loading regime applied on the head of the screws.

Fig. 11 Evolution of the damage pattern caused by loading regimes applied on the pedicle screws head: **a** extension motion; **b** flexion motion; and **c** counter-clockwise axial rotation motion

8 Conclusions

A careful assessment of the fracture patterns and associated mechanisms in a human vertebra after the insertion of pedicle screws was scrutinized by implementing a finite element phase field method. Although the outcomes of the present phase field methodology is in good accordance with numerical studies existing in literature, it is essential to emphasize that confirming the accuracy of such a procedure entails quantitative validation against experimental results. Consequently, an extensive validation, encompassing both clinical and experimental aspects, should be investigated.

Throughout the study, several aspects were pondered to accurately investigate the fractures and crack trajectories, such as maximum peak loads in load versus displacement curves, critical energy release rate, and the characteristic length scale. In particular the computational implementation employed a spatially heterogeneous elastic modulus derived from bone density properties. As a result, a heterogeneous critical energy release rate based on those estimations is derived as well.

The analysis of various fracture types was ensured by conducting a mesh sensitivity study, which provided an optimal mesh size balancing simulation running time and the model's capability to reproduce outcomes within a small relative error. These findings were supported by comparing load versus displacement curves for all considered mesh refinements at the extension vertebral motion mode and a screws insertion angle configuration of $\vec{\alpha} = (-5, 0)$. It is worth mentioning that the damage responses in the vertebra from the developed phase field model are affected when different configurations of the pedicle screws fixation angle are simulated.

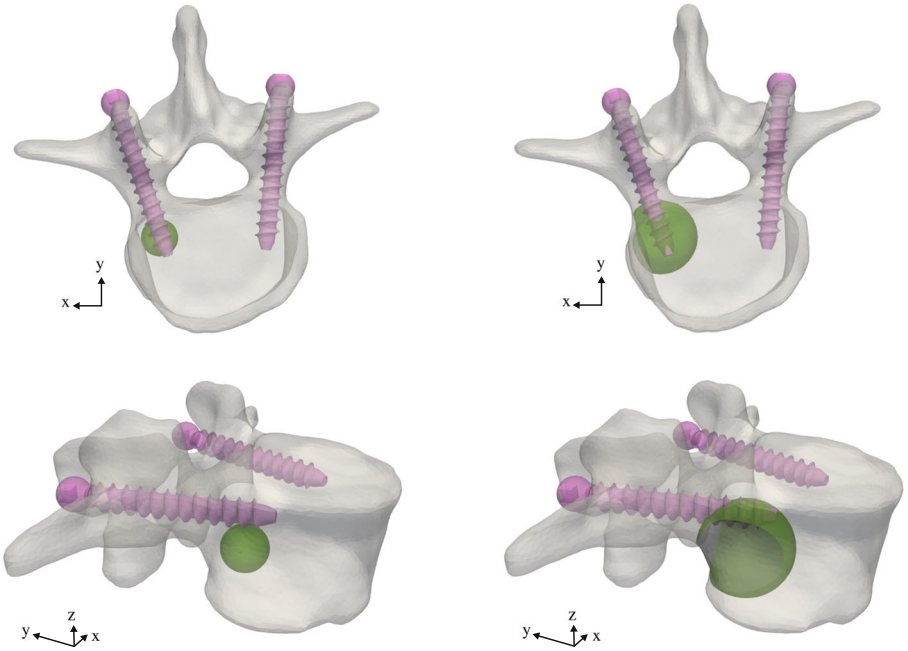

Fig. 12 Perspective and top views of different spherical metastatic lesions centred at the material point (10, 20, 0) in respect to the center of the vertebra-screws model

(a) Vertebral body with a metastatic lesion simulated from a 5 mm radius sphere.

(b) Vertebral body with a metastatic lesion simulated from a 10 mm radius sphere.

In addition, a comparison between phase field finite element approaches was also performed. Essentially, the staggered phase field model makes headway in terms of optimizing computational time consumption in relation to characterizing the damage within the vertebra-screws model, when compared to the results obtained from the monolithic phase field scheme. Last but not least, the phase field method herein implemented could also evaluate the mechanical responses of metastatic vertebra. The results were assessed by analysing osteolytic and osteoblastic metastases, and by varying the size of the lesions. The load versus displacement lines were predicted and the evolution of the fracture patterns have been reported.

Notwithstanding, several potential improvements of the present model can be highlighted. Applications range from spine section models, considering multiple vertebrae and associated stabilization, to the improvement of the material model accounting for multiscale couplings and growth and remodelling both in health and disease. In particular, it is worth mentioning the generalization of the phase field model to incorporate osteon failure mechanics [74] by means multiscale approaches that interact with screws and affect the onset and evolution of a fracture. In such a scenario, concurrent stress rearrangement is obtained, and time-dependent phenomena occur. Additionally, the developed phase-field model can be used in future applications to address a variety of specific problems in bone remodelling and implant biodegradation [75–78]. For example, the model can be used to predict the effects of implant interface biodegradation on bone remodelling, which can help in the design of implants that are more likely to promote bone integration.

Ageing and gender effects are to be addressed in future works [43, 79, 80]. Figure 16 [79] shows the changes in sex hormone levels and bone mass density throughout men's and women's lives. The curves reveal clearly that, in both genders, the bone density is tightly related to testosterone and estrogen levels, and they vary throughout time, i.e. bone mass is steadily decreasing, proving the bone quality deteriorates while ageing. Such aspects might affect the damage patterns of eventual osteon lesions. In [80] numerical simulations on 2D and 3D human femurs to investigate the impact of age and gender on bone mass density variation were conducted. The study revealed three key findings: under intensive loading, bone accelerated formation in various regions; bone density was higher in 20-year-olds, but densification decreased with age, suggesting varying resorption rates; men exhibited a distinct bulk density evolution compared to women, with greater density increase at the femur head to the lower neck. The work proposed a modelling framework for long-term bone density evolution, allowing for the differentiation between genders and age. This model should be incorporated into the model detailed in the present work in order to be predictive for long term scenarios. Starting from the patient reconstruction of the bone density via CT scan, this can be used as an initial condition (together with the additional information on the age and gender of the patient) for the model in [79] to obtain the future density of the bone and apply the presented fracture model.

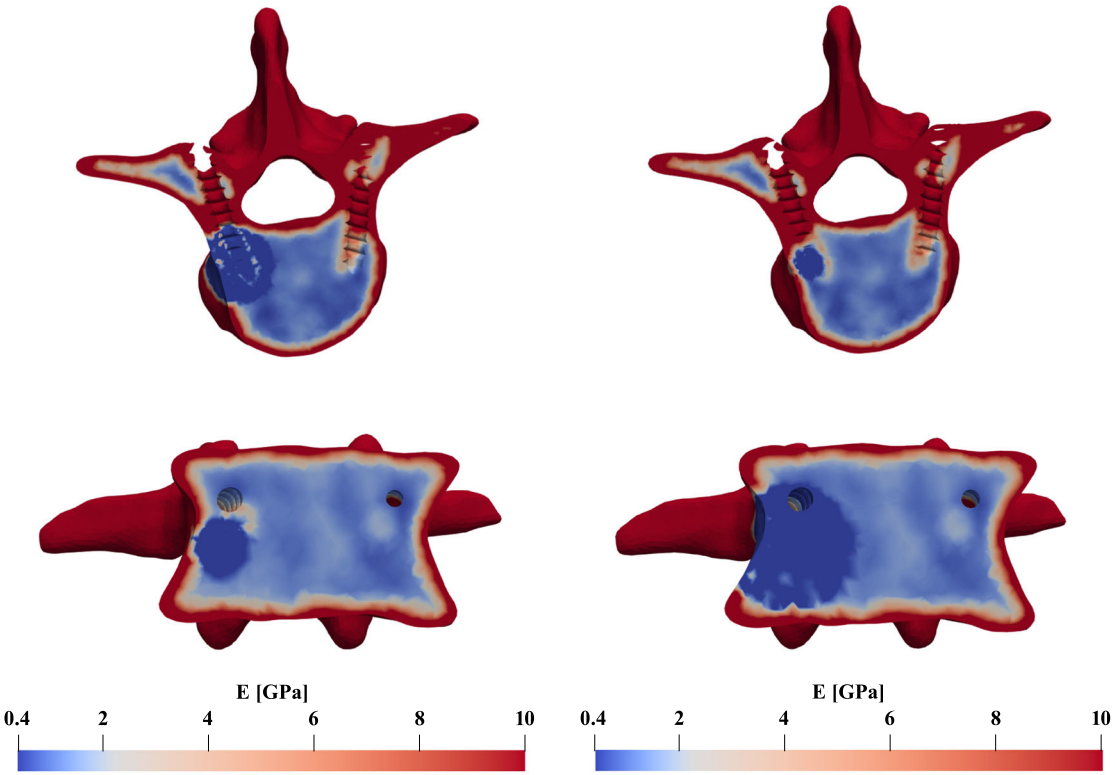

(a) Weakening effect of an osteolytic lesion induced by a 5 mm radius spherical shape.

(b) Weakening effect of an osteolytic lesion induced by 10 mm radius spherical shape.

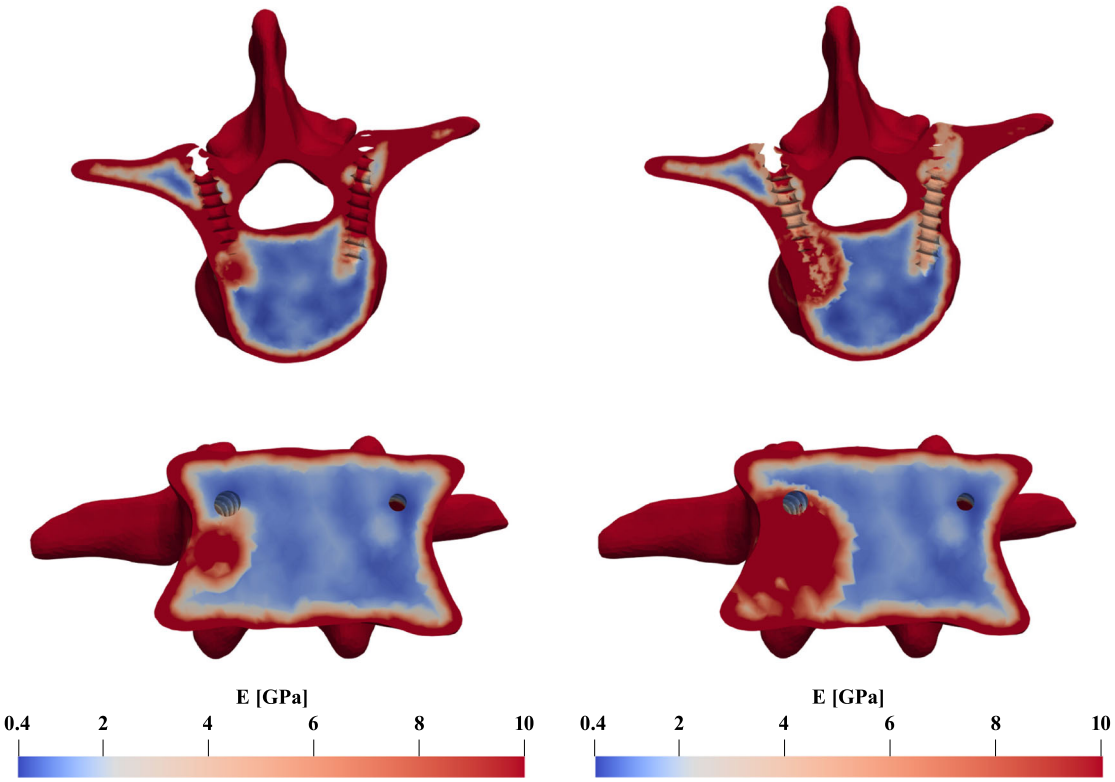

(c) Stiffening effect of an osteoblastic lesion induced by a 5 mm radius spherical shape.

(d) Stiffening effect of an osteoblastic lesion induced by 10 mm radius spherical shape.

Fig. 13 Top and back views of the altered Young's modulus E distribution in the bone induced by spherical osteolytic and osteoblastic metastases

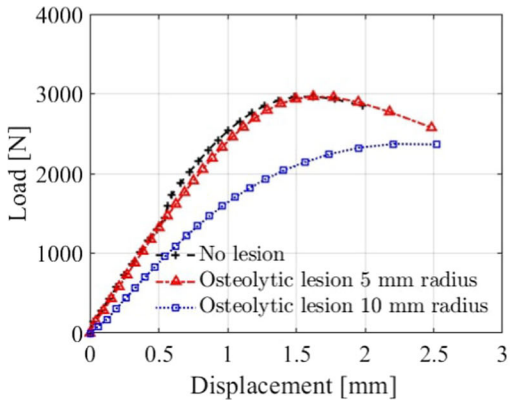

(a) Load vs. Displacement curves obtained from the spherical osteolytic metastasis.

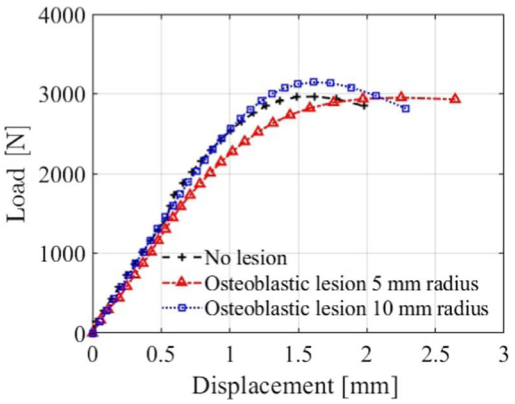

(b) Load vs. Displacement curves obtained from the spherical osteoblastic metastasis.

Fig. 14 Load versus displacement curves obtained for osteolytic and osteoblastic metastases induced by lesions of 5 mm and 10 mm radii centered at the material point (10, 20, 0) in extension movement mode

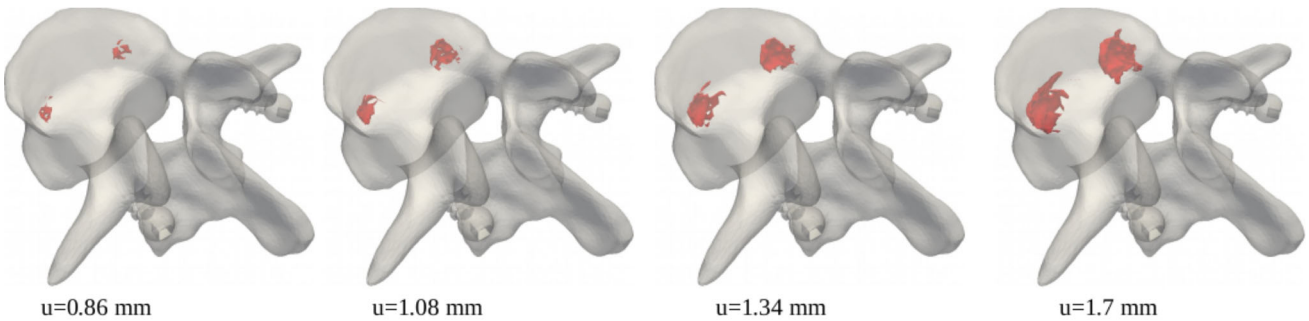

(a) Front view of the evolution of the fracture pattern under vertical flexion loading regime for a osteoblastic lesion induced by a spherical lesion of radius 5 mm.

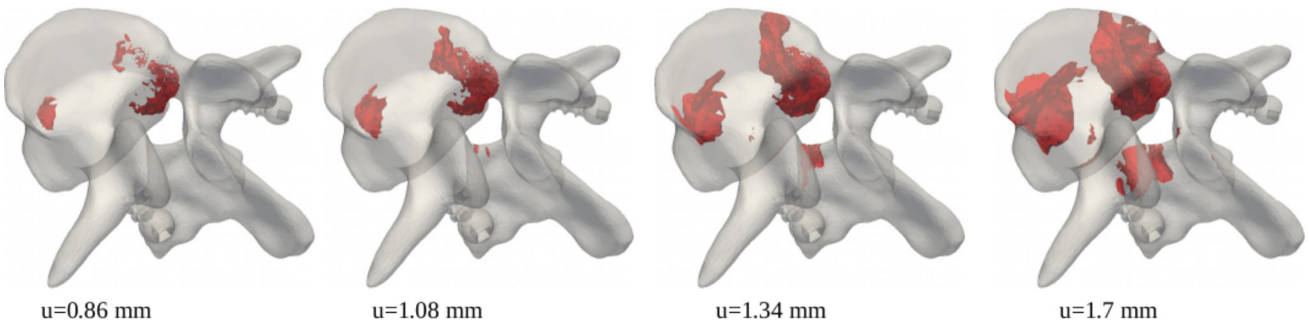

(b) Front view of the evolution of the fracture pattern under vertical flexion loading regime for a osteoblastic lesion induced by a spherical lesion of radius 10 mm.

Fig. 15 Evolution of the damage pattern caused by flexion motion regime for an osteoblastic metastasis

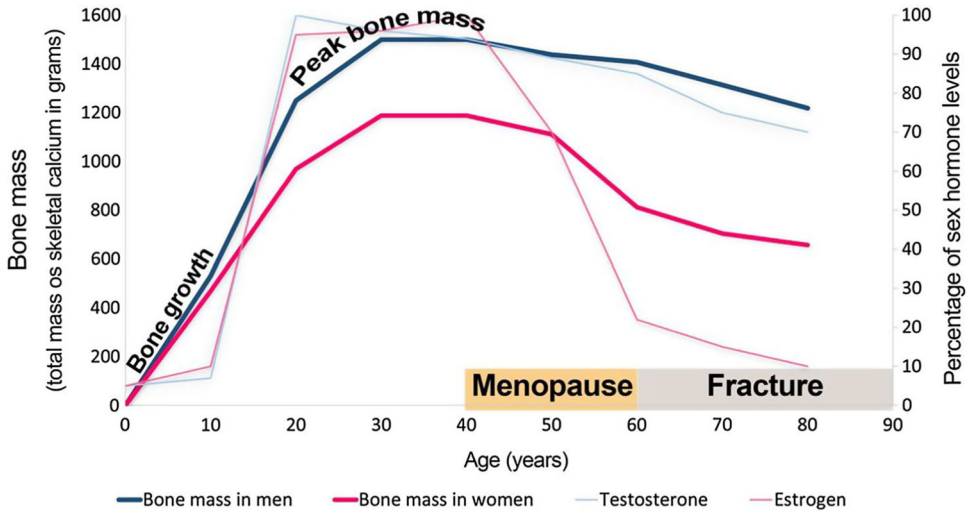

Fig. 16 Diagrammatic representation of the bone mass life-line in both men and women, with the evolution of testosterone levels in men and estrogen levels in women (image taken from [79])

Acknowledgements PL would like to acknowledge financial support from the joint program "Le Scuole Superiori ad Ordinamento Speciale: istituzioni a servizio del Paese", CUP D67G22000130001, through the project "Scientific computing for natural sciences, social sciences, and applications: methodological and technological development". DP acknowledges the support from Istituto Nazionale di Alta Matematica (INdAM), Gruppo Nazionale per la Fisica Matematica (GNFM). AG and DB acknowledge the support of the Italian Ministry for University and Research (MUR), within the PON "Ricerca e Innovazione" 2014–2020 (azione IV.6) - FSEREACT EU and within the project PRIN #2022T3SLAZ, the Italian National Group for Mathematical Physics (GNFMINdAM).

Funding Open access funding provided by Scuola IMT Alti Studi Lucca within the CRUI-CARE Agreement.

References

1. Braides A et al (1998) Approximation of free-discontinuity problems, vol 1694. Springer, Berlin
2. Braides A (2002) Γ-convergence for beginners. Oxford lecture series in mathematics and its applications, vol 22
3. Ambrosio L, Tortorelli VM (1990) Approximation of functional depending on jumps by elliptic functional via Γ-convergence. Commun Pure Appl Math 43(8):999–1036
4. Ambrosio L (1992) On the approximation of free discontinuity problems. Boll Un Mat Ital B 7:105–123
5. Francfort GA, Marigo J-J (1998) Revisiting brittle fracture as an energy minimization problem. J Mech Phys Solids 46(8):1319–1342
6. Bazant ZP (1982) Crack band model for fracture of geomaterials. pp 1137–1152, AA Balkema
7. Bažant ZP, Lin F-B (1988) Nonlocal smeared cracking model for concrete fracture. J Struct Eng 114(11):2493–2510
8. Bazant Z, Jirasek M (1994) Damage nonlocality due to microcrack interactions: statistical determination of crack influence function. Fracture and damage in Quasibrittle structures, pp 3–17
9. Gerard B, Pijaudier-Cabot G, Laborderie C (1998) Coupled diffusion-damage modelling and the implications on failure due to strain localisation. Int J Solids Struct 35(31–32):4107–4120
10. Geers M, De Borst R, Brekelmans W, Peerlings R (1998) Strain-based transient-gradient damage model for failure analyses. Comput Methods Appl Mech Eng 160(1–2):133–153
11. Bourdin B, Francfort GA, Marigo J-J (2000) Numerical experiments in revisited brittle fracture. J Mech Phys Solids 48(4):797–826
12. Bourdin B, Francfort GA, Marigo J-J (2008) The variational approach to fracture. J Elast 91(1):5–148
13. Kuhn C, Müller R (2008) A phase field model for fracture. In: PAMM: proceedings in applied mathematics and mechanics. Wiley Online Library, vol 8, pp 10223–10224
14. Hakim V, Karma A (2009) Laws of crack motion and phase-field models of fracture. J Mech Phys Solids 57(2):342–368
15. Amor H, Marigo J-J, Maurini C (2009) Regularized formulation of the variational brittle fracture with unilateral contact: numerical experiments. J Mech Phys Solids 57(8):1209–1229
16. Nguyen TT, Yvonnet J, Zhu Q-Z, Bornert M, Chateau C (2015) A phase field method to simulate crack nucleation and propagation in strongly heterogeneous materials from direct imaging of their microstructure. Eng Fract Mech 139:18–39
17. Msekh MA, Sargado JM, Jamshidian M, Areias PM, Rabczuk T (2015) Abaqus implementation of phase-field model for brittle fracture. Comput Mater Sci 96:472–484
18. Jodlbauer D, Langer U, Wick T (2020) Parallel matrix-free higher-order finite element solvers for phase-field fracture problems. Math Comput Appl 25(3):40
19. Wu J-Y (2017) A unified phase-field theory for the mechanics of damage and quasi-brittle failure. J Mech Phys Solids 103:72–99
20. Miehe C, Hofacker M, Welschinger F (2010) A phase field model for rate-independent crack propagation: robust algorithmic imple-

mentation based on operator splits. Comput Methods Appl Mech Eng 199(45–48):2765–2778
21. Miehe C, Welschinger F, Hofacker M (2010) Thermodynamically consistent phase-field models of fracture: variational principles and multi-field FE implementations. Int J Numer Meth Eng 83(10):1273–1311
22. Tanné E, Li T, Bourdin B, Marigo J-J, Maurini C (2018) Crack nucleation in variational phase-field models of brittle fracture. J Mech Phys Solids 110:80–99
23. Bianchi D, Falcinelli C, Molinari L, Gizzi A, Di Martino A (2022) Osteolytic vs. osteoblastic metastatic lesion: Computational modeling of the mechanical behavior in the human vertebra after screws fixation procedure. J Clin Med 11(10):2850
24. Fritsch A, Hellmich C (2007) "universal" microstructural patterns in cortical and trabecular, extracellular and extravascular bone materials: micromechanics-based prediction of anisotropic elasticity. J Theor Biol 244(4):597–620
25. Bokov A et al (2016) Pedicle screw loosening prediction in patients with degenerative diseases of lumbar spine using bone density measured in hounsfield units. J Osteoporos Phys Act 4(1):1–4
26. Nguyen L, Stoter S, Baum T, Kirschke J, Ruess M, Yosibash Z, Schillinger D (2017) Phase-field boundary conditions for the voxel finite cell method: Surface-free stress analysis of ct-based bone structures. Int J Numer Methods Biomed Eng 33(12):e2880
27. Shen R, Waisman H, Yosibash Z, Dahan G (2019) A novel phase field method for modeling the fracture of long bones. Int J Numer Methods Biomed Eng 35(8):e3211
28. Maghami E, Moore JP, Josephson TO, Najafi AR (2022) Damage analysis of human cortical bone under compressive and tensile loadings. Comput Methods Biomech Biomed Engin 25(3):342–357
29. Sterba W, Kim D-G, Fyhrie DP, Yeni YN, Vaidya R (2007) Biomechanical analysis of differing pedicle screw insertion angles. Clin Biomech 22(4):385–391
30. Sansur CA, Caffes NM, Ibrahimi DM, Pratt NL, Lewis EM, Murgatroyd AA, Cunningham BW (2016) Biomechanical fixation properties of cortical versus transpedicular screws in the osteoporotic lumbar spine: an in vitro human cadaveric model. J Neurosurg Spine 25(4):467–476
31. Incorrect spinal stabilization intervention in a 70 years old female patient in lucca-italy. https://avvocaticollegati.it/2023/02/28/errato-intervento-alla-colonna-vertebrale/. Accessed: 01-12-2023
32. Ohba T, Ebata S, Oba H, Koyama K, Haro H (2019) Risk factors for clinically relevant loosening of percutaneous pedicle screws. Spine Surg Related Res 3(1):79–85
33. Inceoğlu S, Montgomery WH, Clair SS, McLain RF (2011) Pedicle screw insertion angle and pullout strength: comparison of 2 proposed strategies. J Neurosurg Spine 14(5):670–676
34. Molinari L, Falcinelli C, Gizzi A, Martino AD (2021) Biomechanical modeling of metal screw loadings on the human vertebra. Acta Mech Sin 37(2):307–320
35. Molinari L, Falcinelli C, Gizzi A, Di Martino A (2021) Effect of pedicle screw angles on the fracture risk of the human vertebra: a patient-specific computational model. J Mech Behav Biomed Mater 116:104359
36. Yosibash Z, Tal D, Trabelsi N (2010) Predicting the yield of the proximal femur using high-order finite-element analysis with inhomogeneous orthotropic material properties. Philos Trans R Soc A Math Phys Eng Sci 368(1920):2707–2723
37. Matsuura Y, Giambini H, Ogawa Y, Fang Z, Thoreson A, Yaszemski M, Lu L, An K (2014) Specimen-specific nonlinear finite element modeling to predict vertebrae fracture loads after vertebroplasty. Spine 39(22):E1291
38. Denaro V, Di Martino A (2019) Spinal metastases: diagnosis and management. Springer, Cham, pp 137–147
39. Costa M, Eltes P, Lazary A, Varga P, Viceconti M, Dall'Ara E (2019) Biomechanical assessment of vertebrae with lytic metastases with subject-specific finite element models. J Mech Behav Biomed Mater 98(4):268–290
40. Alnæs MS, Hake J, Kirby RC, Langtangen HP, Logg A, Wells GN (2011) The fenics manual. FEniCS Project, version October 31st, vol 36
41. Pongiman R (2014) HyperMesh introduction pre-processing for finite element analysis. Altair University, Troy
42. Geuzaine C, Remacle J-F (2009) Gmsh: A 3-D finite element mesh generator with built-in pre-and post-processing facilities. Int J Numer Meth Eng 79(11):1309–1331
43. Nalla RK, Kruzic JJ, Kinney JH, Ritchie RO (2004) Effect of aging on the toughness of human cortical bone: evaluation by r-curves. Bone 35(6):1240–1246
44. Fields AJ, Lee GL, Keaveny TM (2010) Mechanisms of initial endplate failure in the human vertebral body. J Biomech 43(16):3126–3131
45. Erdem I, Truumees E, van der Meulen MC (2013) Simulation of the behaviour of the L1 vertebra for different material properties and loading conditions. Comput Methods Biomech Biomed Eng 16(7):736–746
46. Song K, Wang Z, Lan J, Ma S (2021) Porous structure design and mechanical behavior analysis based on TPMS for customized root analogue implant. J Mech Behav Biomed Mater 115:104222
47. Aufa A, Hassan MZ, Ismail Z (2022) Recent advances in Ti-6Al-4V additively manufactured by selective laser melting for biomedical implants: prospect development. J Alloy Compd 896:163072
48. Bartsch K, Herzog D, Bossen B, Emmelmann C (2021) Material modeling of Ti-6Al-4V alloy processed by laser powder bed fusion for application in macro-scale process simulation. Mater Sci Eng, A 814:141237
49. Del Piero G, Lancioni G, March R (2007) A variational model for fracture mechanics: numerical experiments. J Mech Phys Solids 55(12):2513–2537
50. Arroyo M, Ortiz M (2006) Local maximum-entropy approximation schemes: a seamless bridge between finite elements and meshfree methods. Int J Numer Meth Eng 65(13):2167–2202
51. Hofacker M, Miehe C (2013) A phase field model of dynamic fracture: Robust field updates for the analysis of complex crack patterns. Int J Numer Meth Eng 93(3):276–301
52. Miehe C, Schaenzel L-M, Ulmer H (2015) Phase field modeling of fracture in multi-physics problems. Part I. Balance of crack surface and failure criteria for brittle crack propagation in thermo-elastic solids. Comput Methods Appl Mech Eng 294:449–485
53. Miehe C, Hofacker M, Schänzel L-M, Aldakheel F (2015) Phase field modeling of fracture in multi-physics problems. Part II. coupled brittle-to-ductile failure criteria and crack propagation in thermo-elastic-plastic solids. Comput Methods Appl Mech Eng 294:486–522
54. Nguyen T-T, Yvonnet J, Zhu Q-Z, Bornert M, Chateau C (2016) A phase-field method for computational modeling of interfacial damage interacting with crack propagation in realistic microstructures obtained by microtomography. Comput Methods Appl Mech Eng 312:567–595
55. Coleman BD, Noll W (1974) The thermodynamics of elastic materials with heat conduction and viscosity. In: The foundations of mechanics and thermodynamics. Springer, pp 145–156
56. Wambacq J, Ulloa J, Lombaert G, François S (2021) Interior-point methods for the phase-field approach to brittle and ductile fracture. Comput Methods Appl Mech Eng 375:113612
57. Ambati M, Gerasimov T, De Lorenzis L (2015) A review on phase-field models of brittle fracture and a new fast hybrid formulation. Comput Mech 55:383–405
58. Dreischarf M, Zander T, Shirazi-Adl A, Puttlitz C, Adam C, Chen C, Goel V, Kiapour A, Kim Y, Labus K et al (2014) Comparison

of eight published static finite element models of the intact lumbar spine: predictive power of models improves when combined together. J Biomech 47(8):1757–1766
59. Matsukawa K, Yato Y, Imabayashi H, Hosogane N, Asazuma T, Nemoto K (2015) Biomechanical evaluation of the fixation strength of lumbar pedicle screws using cortical bone trajectory: a finite element study. J Neurosurg Spine 23(4):471–478
60. Gustafsson A, Wallin M, Isaksson H (2019) Age-related properties at the microscale affect crack propagation in cortical bone. J Biomech 95:109326
61. Hug L, Dahan G, Kollmannsberger S, Rank E, Yosibash Z (2022) Predicting fracture in the proximal humerus using phase field models. J Mech Behav Biomed Mater 134:105415
62. Chan KS, Chan CK, Nicolella DP (2009) Relating crack-tip deformation to mineralization and fracture resistance in human femur cortical bone. Bone 45(3):427–434
63. Koester K, Barth H, Ritchie R (2011) Effect of aging on the transverse toughness of human cortical bone: evaluation by R-curves. J Mech Behav Biomed Mater 4(7):1504–1513
64. Zhang X, Vignes C, Sloan SW, Sheng D (2017) Numerical evaluation of the phase-field model for brittle fracture with emphasis on the length scale. Comput Mech 59:737–752
65. Pham K, Amor H, Marigo J-J, Maurini C (2011) Gradient damage models and their use to approximate brittle fracture. Int J Damage Mech 20(4):618–652
66. Martínez-Pañeda E, Golahmar A, Niordson CF (2018) A phase field formulation for hydrogen assisted cracking. Comput Methods Appl Mech Eng 342:742–761
67. Préve D, Lenarda P, Maskery I, Paggi M (2023) A comprehensive characterization of fracture in unit cell open foams generated from triply periodic minimal surfaces. Eng Fract Mech 277:108949
68. Zysset PK, Guo XE, Hoffler CE, Moore KE, Goldstein SA (1999) Elastic modulus and hardness of cortical and trabecular bone lamellae measured by nanoindentation in the human femur. J Biomech 32(10):1005–1012
69. Gustafsson A, Wallin M, Khayyeri H, Isaksson H (2019) Crack propagation in cortical bone is affected by the characteristics of the cement line: a parameter study using an XFEM interface damage model. Biomech Model Mechanobiol 18(4):1247–1261
70. Gustafsson A, Isaksson H (2022) Phase field models of interface failure for bone application-evaluation of open-source implementations. Theor Appl Fract Mech 121:103432
71. Paggi M, Reinoso J (2017) Revisiting the problem of a crack impinging on an interface: a modeling framework for the interaction between the phase field approach for brittle fracture and the interface cohesive zone model. Comput Methods Appl Mech Eng 321:145–172
72. Kumar PAV, Dean A, Reinoso J, Lenarda P, Paggi M (2021) Phase field modeling of fracture in functionally graded materials: Γ-convergence and mechanical insight on the effect of grading. Thin-Walled Struct 159:107234
73. Costa M, Campello LB, Ryan M, Rochester J, Viceconti M, Dall'Ara E (2020) Effect of size and location of simulated lytic lesions on the structural properties of human vertebral bodies, a micro-finite element study. Bone Rep 12:100257
74. Gaziano P, Monaldo E, Falcinelli C, Vairo G (2022) Elasto-damage mechanics of osteons: a bottom-up multiscale approach. J Mech Phys Solids 167:104962
75. Hermann A, Shojaei A, Steglich D, Höche D, Zeller-Plumhoff B, Cyron CJ (2022) Combining peridynamic and finite element simulations to capture the corrosion of degradable bone implants and to predict their residual strength. Int J Mech Sci 220:107143
76. Steglich D, Besson J, Reinke I, Helmholz H, Luczak M, Garamus VM, Wiese B, öche DH, Cyron CJ, Willumeit-Römer R (2023) Strength and ductility loss of magnesium-gadolinium due to corrosion in physiological environment: experiments and modeling. J Mech Behav Biomed Mater 144:105939
77. Gizzi A, Cyron CJ, Falcinelli C, Vasta M (2024) Evolution of fiber distributions in homogenized constrained mixture models of soft tissue growth and remodeling: Uniaxial loading. J Mech Phys Solids 183:105491
78. Sardhara T, Shkurmanov A, Li Y, Shi S, Cyron CJ, Aydin RC, Ritter M (2024) Role of slice thickness quantification in the 3d reconstruction of fib tomography data of nanoporous materials. Ultramicroscopy 256:113878
79. Ober C, Loisel DA, Gilad Y (2008) Sex-specific genetic architecture of human disease. Nat Rev Genet 9(12):911–922
80. Barkaoui A, Ben Kahla R, Merzouki T, Hambli R (2017) Age and gender effects on bone mass density variation: finite elements simulation. Biomech Model Mechanobiol 16:521–535